JGR Solid Earth

RESEARCH ARTICLE
10.1029/2021JB022839

Special Section:
Understanding and anticipating Induced Seismicity: from mechanics to seismology

Raton Basin Induced Seismicity Is Hosted by Networks of Short Basement Faults and Mimics Tectonic Earthquake Statistics

M. Glasgow[1], B. Schmandt[1], R. Wang[1], M. Zhang[2], S. L. Bilek[3], and E. Kiser[4]

[1]Department of Earth and Planetary Sciences, University of New Mexico, Albuquerque, NM, USA, [2]Department of Earth and Environmental Sciences, Dalhousie University, Halifax, NS, Canada, [3]Department of Earth and Environmental Science, New Mexico Institute of Mining and Technology, Socorro, NM, USA, [4]Department of Geosciences, University of Arizona, Tucson, AZ, USA

Key Points:

- Seismicity is hosted by short, <3 km long, reactivated basement faults with variable strikes and faulting styles
- The fault zone that hosted a M_w 5.3 event in 2011 exhibits low seismicity following an 80% reduction of the wastewater-injection rate
- Similarity of spatiotemporal-magnitude basin statistics to tectonic sequences suggests earthquakes mainly release stored tectonic stress

Supporting Information:

Supporting Information may be found in the online version of this article.

Correspondence to:

M. Glasgow,
mglasgow@unm.edu

Citation:

Glasgow, M., Schmandt, B., Wang, R., Zhang, M., Bilek, S. L., & Kiser, E. (2021). Raton Basin induced seismicity is hosted by networks of short basement faults and mimics tectonic earthquake statistics. *Journal of Geophysical Research: Solid Earth*, *126*, e2021JB022839. https://doi.org/10.1029/2021JB022839

Received 16 JUL 2021
Accepted 1 NOV 2021

Abstract The Raton Basin has been an area of injection induced seismicity for the past two decades. Previously, the reactivated fault zone structures and spatiotemporal response of seismicity to evolving injection have been poorly constrained due to sparse publicly available seismic monitoring. The application of a machine-learning phase picker to 4 years of continuous seismic data from a local array enables the detection and location of ~38,000 earthquakes. The events from 2016 to 2020 are ~2.5–6 km below sea level and range from $M_L < -1$ to 4.2. Most earthquakes occur within previously identified ~N-S zones of seismicity, however our new catalog illuminates that these zones are composed of many short faults with variable orientations. The two most active zones, the Vermejo Park and Tercio zones, are potentially linked by small intermediate faults. In total, we find ~60 short (<3 km long) basement faults with strikes from WNW to NNE. Faulting mechanisms are predominantly normal but some variability, including reverse dip-slip and oblique-slip, is observed. The Trinidad fault zone, which previously hosted a M_w 5.3 earthquake in 2011, is quiescent during 2016–2020, likely in response to both slow accumulation of tectonic strain after the 2011 sequence, and the significant decrease (80% reduction) in nearby wastewater injection from 2012 to 2016. Unlike some other regions, where induced seismicity was triggered in response to higher injection rates, the Raton Basin's frequency-magnitude and spatiotemporal statistics are not distinguishable from tectonic seismicity. The similarity suggests that seismicity in the Raton Basin is predominantly releasing tectonic stress.

Plain Language Summary The Raton Basin, located on the Colorado-New Mexico border, has a low level of historical seismicity but experienced a significant increase of earthquakes in the past two decades, coinciding with increased wastewater injection and coal-bed methane production. We use four years of continuous local seismic data to detect ~38,000 earthquakes from 2016 to 2020. We find that the previously identified 10–20 km long zones of seismicity are composed of many shorter faults, <3 km long, with variable orientations and slip mechanisms. We observed very little seismicity in the zone that previously hosted the largest earthquake (M_w 5.3 in 2011) in the basin and attribute this finding to both the slow accumulation of tectonic strain following the 2011 sequence and the significant decrease (80% reduction) of wastewater injection to this zone from 2012 to 2016. Overall, the frequency-magnitude and spatial-temporal earthquake behavior of the Raton Basin is not distinguishable from tectonic seismicity. This statistical similarity suggests Raton Basin seismicity predominantly releases tectonic stress accumulated over geologic time.

1. Introduction

Human-induced earthquakes present societally relevant hazards and opportunities to study earthquake sequences and seismogenic structures in the central United States at accelerated time scales. The abrupt rise of human-induced earthquakes in the central U.S. began in 2009 and peaked in 2015 (Figure 1a; Keranen & Weingarten, 2018; Langenbruch et al., 2018; Weingarten et al., 2015). Wastewater injection from oil and gas operations is the main driver behind the observed seismicity (e.g., Ellsworth, 2013; Keranen et al., 2014; Weingarten et al., 2015). Since 2015, seismicity decreased on average for the central U.S. and decreased or plateaued for the strongest contributing regions, example, central Oklahoma and Arkansas (Langenbruch

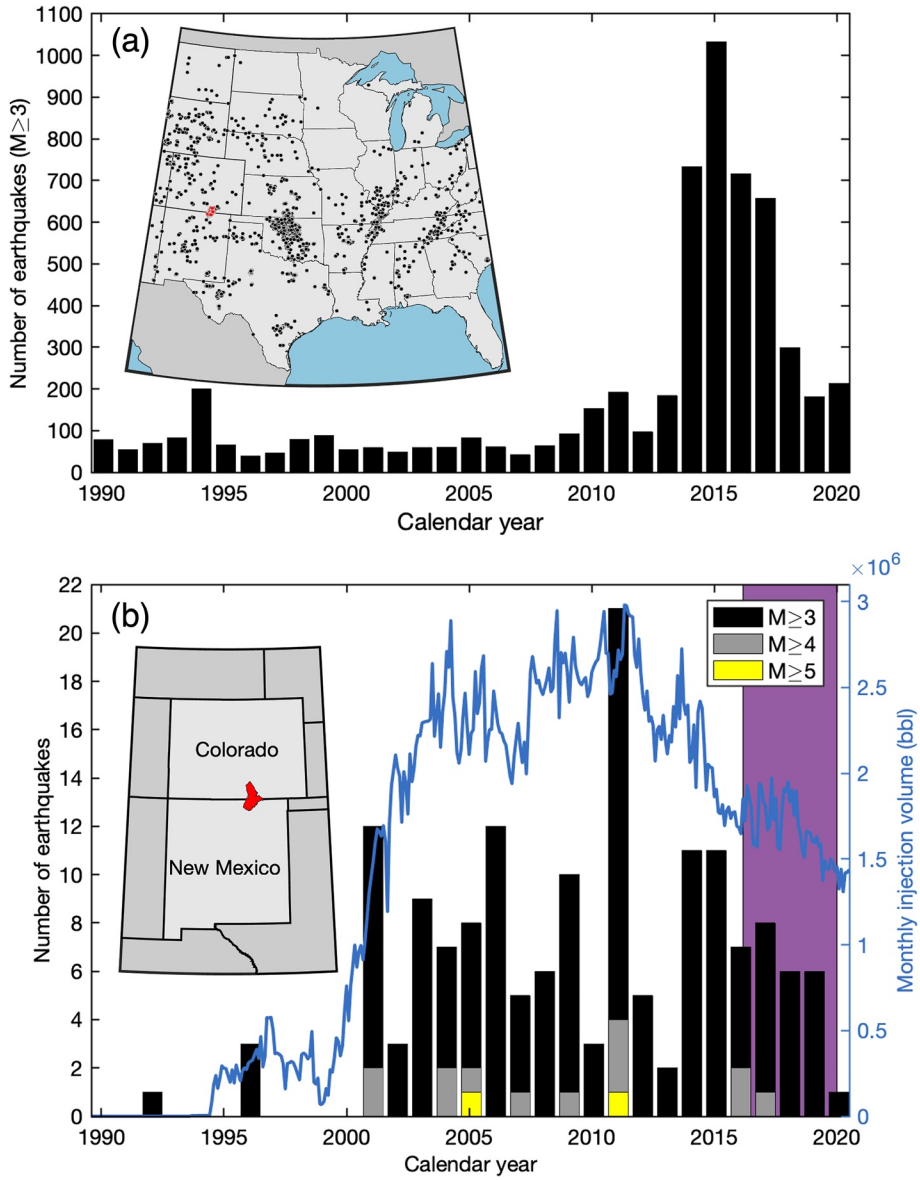

Figure 1. (a) Yearly number of M ≥ 3 earthquakes in the central United States (ANSS ComCat, 2021). Inset displays map of the central United States with M ≥ 3 earthquakes (circles). Red circles indicate earthquakes in the Raton Basin. (b) Yearly number of M ≥ 3 earthquakes in the Raton Basin. See legend for magnitude details. Monthly injection volume (blue line) is on the right *y*-axis (COGCC, 2021; NMOCD, 2021). Injection is summed across the 24–29 wells typically operating in the basin. Our study period from July 2016 to July 2020 is highlighted in purple. Inset displays state borders and the Raton Basin in red.

et al., 2018; Scanlon et al., 2019). However, a few regions have expanded oil and gas operations in recent years and are experiencing a rise in seismicity, example, west Texas and southeastern New Mexico (Frohlich et al., 2020; Skoumal & Trugman, 2021; Skoumal et al., 2020). Studying how seismicity evolves following the peak of wastewater injection may be informative for other regions that experience similar situations in the future.

The Raton Basin located on the Colorado-New Mexico border is one of the regions in the central United States where seismicity ramped up in concert with wastewater injection (Figure 1b; Rubinstein et al., 2014). Coal-bed methane production and wastewater injection began in 1994 and its increase from ~2000 to 2002 was accompanied by a rapid increase in seismicity (Figure 1b; Advanced National Seismic System Comprehensive Earthquake Catalog (ANSS ComCat)). Thus, the Raton Basin's rise of induced seismicity was

~8 years ahead of the central U.S. average (Figure 1), and it is a valuable example of how induced seismicity can persist as injection decreases or potentially cease on local scales (e.g., Healy et al., 1968; Hsieh & Bredehoeft, 1981; Bollinger, et al., 1983). Historically, seismicity in the basin was rare but not absent. Rubinstein et al. (2014) estimated a magnitude of completeness of 3.8 for the Raton Basin from 1970 to 2011. One $M \geq 4$ earthquake occurred from 1970 to 2000 and 15 $M \geq 4$ earthquakes occurred from 2001 to 2020 (ANSS ComCat, 2021; Rubinstein et al., 2014). The rate of $M \geq 3$ earthquakes in the basin began increasing in 2001 and peaked at 20 $M \geq 3$ earthquakes in 2011. The largest earthquake of the region was the 2011 M_w 5.3 event (Barnhart et al., 2014; Rubinstein et al., 2014). Since 2011, seismicity has decreased to an average of ~6 $M \geq 3$ earthquakes/year but remains much higher than prior to 2001 (Figure 1). Most recently, the region has experienced some of the lowest rates of seismicity since 2001, with an average of 1.7 $M \geq 3$ earthquakes/year from January 2020 to September 2021 (ANSS ComCat, 2021).

The disposal of fluids, generally byproducts of oil and gas production, by injection is the main driver of increased seismicity in the central United States (e.g., Ellsworth, 2013; Keranen et al., 2014; Weingarten et al., 2015). Pore pressure changes are often considered the dominant mechanism for inducing earthquakes but poroelastic coupling can also play an important role (Segall & Lu, 2015). Wastewater injection near faults can increase the pore pressure and reduce the effective normal stress on a fault thereby promoting fault slip (Hsieh & Bredehoeft, 1981; Raleigh et al., 1976). Poroelasticity can amplify the stress changes potentially leading to an increase in both the seismic rate (Zhai et al., 2019) and seismic footprint (Goebel & Brodsky, 2018). In cases where hydraulic communication between faults and seismicity is weak or uncertain, poroelastic stress may be more effective than pore pressure diffusion at earthquake triggering, example, earthquakes on low permeability faults (Chang & Segall, 2016) or for far-field earthquakes (Goebel et al., 2017). Studies of induced seismicity in the central United States demonstrate that small pressure changes, example, <0.1 MPa, can induce earthquakes (Keranen et al., 2014; Nakai, Weingarten, et al., 2017; Verdecchia et al., 2021). In Oklahoma, and southern Kansas, the majority of induced earthquakes occur in the basement beneath the injection reservoir (Schoenball et al., 2018; Walsh & Zoback, 2015). Precambrian basement faults extend upward into the primary wastewater disposal unit providing likely hydraulic pathways for downward migration of pore fluid pressure (Schwab et al., 2017). Earthquakes also occur in the basement in the Raton Basin (Nakai, Weingarten, et al., 2017). It is less certain how pore pressure is transmitted from the injection reservoir to the basement, but permeable faults have been hypothesized (Nakai, Weingarten, et al., 2017; Rubinstein et al., 2014).

Injection rate and cumulative injected volume are proposed as key parameters that influence induced seismicity in the United States (McGarr, 2014; Scanlon et al., 2019; Weingarten et al., 2015). High-rate injection wells (≥300,000 barrels/month) are associated with earthquakes twice as often as low-rate injection wells (<100,000 barrels/month) in the central and eastern United States (Weingarten et al., 2015). Scanlon et al. (2019) found the association of earthquakes to cumulative wastewater injection volume remained random below 1 million barrels (Mbbl) per well and increased from 60% at 1 Mbbl/well to ~90–100% at ≥30 Mbbl/well. Wastewater injection wells in the Raton Basin inject at a range of rates from high to low (≥300,000–<100,000 bbl/month). The average injection rate in the basin since 2001 is low (~80,000–90,000 bbl/month per well) but the long injection history yields high cumulative injection volumes, ~22 Mbbl/well since 1994. Most recently, the basin has experienced a decline in the wastewater injection rate and volume (Figure 1b). The average rate for the ~10-year plateau of injection from 2004 to 2014 was ~2.45 Mbbl/month, whereas the rate from 2016 to 2021 is ~1.67 Mbbl/month.

Publicly available seismic data near the Raton Basin have been sparse, apart from the temporary aftershock deployments in 2001 and 2011 (Meremonte et al., 2002; Rubinstein et al., 2014) and the EarthScope Transportable Array during which two stations bounded the basin from 2008 to 2010 (Nakai, Sheehan, et al., 2017; Nakai, Weingarten, et al., 2017). Previous seismic studies identified three prominent zones of seismicity (Figure 2), referred to as the Trinidad (Barnhart et al., 2014; Rubinstein et al., 2014), Vermejo Park, and Tercio zones (Nakai, Weingarten, et al., 2017). The Trinidad zone strikes NE–SW, extends ~15 km, and hosted the largest recorded earthquake within the basin, a M_w 5.3 in 2011 (Rubinstein et al., 2014). The Vermejo Park and Tercio zones strike N-S and extend ~20 and ~10 km, respectively (Nakai, Weingarten, et al., 2017). It is unclear if these zones are spanned by continuous faults. Recent research utilizing a dense one-month array deployed in a subset of the Raton Basin suggests that more complex fault networks exist

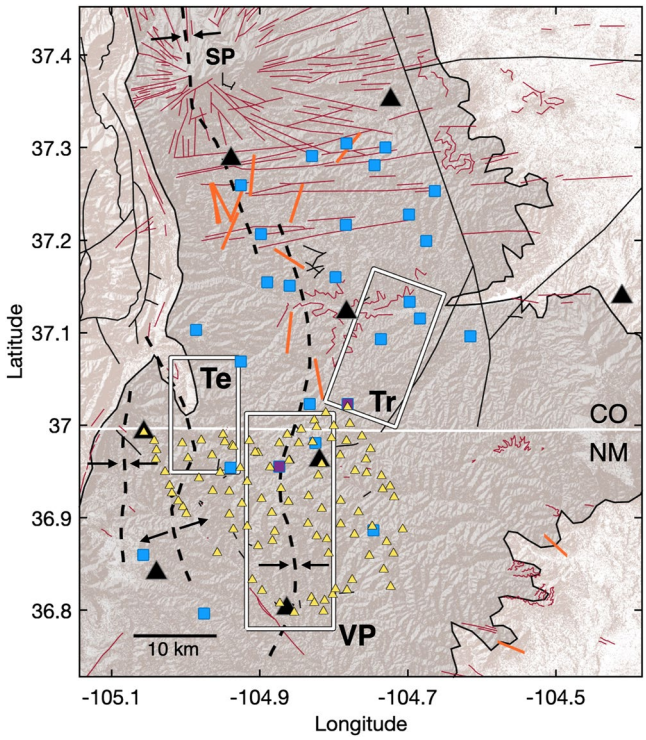

Figure 2. Map of study region. The Raton Basin is outlined in black and shaded gray. The map displays the eight broadband seismometers (black triangles), 96 geophone nodes (yellow triangles), and 29 wastewater injection wells (blue squares) used in this study. Purple squares indicate co-located wastewater injection wells. The three white boxes approximate previously identified zones of seismicity from Rubinstein et al. (2014) and Nakai, Weingarten, et al. (2017). They are abbreviated Te—Tercio, Tr—Trinidad, and VP—Vermejo Park. Geologic features include mapped surface faults (black lines), mapped dikes and sills (red lines), and anticlines and synclines (dashed black lines; Papadopulous & Associates, Inc., 2008; Pillmore, 1964, 1965a, 1965b, 1969, 2003; Stoeser et al., 2007; Johnson, 1969). The Spanish Peaks are labeled SP. Orange lines are maximum horizontal stress orientations from Lund Snee and Zoback (2020).

within the previously identified zones of seismicity (Wang, Schmandt et al., 2020).

Deployment and continuous operation of a local broadband array since 2016 (Figure 2) creates the opportunity to advance knowledge of the structural setting and the spatiotemporal characteristics of Raton Basin seismicity in the context of post-peak wastewater injection. A new high-resolution earthquake catalog was built by taking advantage of a machine-learning phase picker (Zhu & Beroza, 2019) and a waveform correlation-based hypocenter estimation method (Trugman & Shearer, 2017) to investigate four years of continuous seismic data. The new catalog of ~38,000 events is quantitatively analyzed to constrain the geometry of reactivated faults, whose diverse orientations are supported by complementary focal mechanism analysis. Spatiotemporal-magnitude statistics are calculated for multiple sections of the basin and compared to results from tectonic and other induced settings to evaluate potential drivers of Raton Basin seismicity.

2. Geologic Background

The Raton Basin is asymmetric with the synclinal axis west of center (Johnson & Finn, 2001). The western margin dips steeply east toward the Sangre de Cristo Mountains, whereas the eastern margin tilts gently west (Baltz, 1965; Flores & Bader, 1999; Johnson & Finn, 2001; Woodward, 1997). The Devonian through Plio-Pleistocene basin stratigraphy is underlain by Precambrian basement (Johnson & Finn, 2001). The basin is defined by the area contained within the Trinidad sandstone and Vermejo formation contact (Figure 2; Hemborg, 1998). East-west compression during the Laramide orogeny (late Cretaceous to early Tertiary) resulted in predominantly ~N-S oriented faults and fold axes (Woodward, 1997). Igneous activity during the mid to late Tertiary emplaced dikes, sills, and laccoliths along the weak zones created during the Laramide orogeny (Johnson, 1969; Johnson & Wood, 1956; Woodward, 1997). The widespread intrusive activity includes over 80 mapped dikes and sills (Dane & Bachman, 1965, Johnson, 1969; Woodward, 1997) and the Spanish Peaks (Figure 2) towering over the basin with ~1.5 km of topographic relief (Johnson & Finn, 2001). Igneous intrusions and faults can impact fluid flow by acting as either permeable paths or impermeable barriers. Hemborg (1998) suggests faulting and intrusions in the northern Raton Basin may have enhanced the permeability of coal reservoirs and notes that higher performing wells are closer to faults.

The Raton Basin is located at the intersection of two major stress fields, the N-S normal faulting extensional stress field of the Rio Grande Rift and the E-W strike-slip compressive stress field of the broader central United States (Lund Snee & Zoback, 2020). This convergence produces a range of stress orientations, from NE-SW to NW-SE maximum horizontal stress, in and along the margins of the basin (Figure 2). Earthquake focal mechanisms support predominantly normal dip-slip and occasional strike-slip motion near the central basin (Barnhart et al., 2014; Saint Louis University, 2021; U.S. Geological Survey, 2021; Wang, Schmandt et al., 2020). Similar to the neighboring Rio Grande Rift and southern Rocky Mountains, the Raton Basin has high heat flow, ~90–165 mW/m^2 on average compared to ~65 mW/m^2 for the global continental average (Blackwell et al., 2011; Morgan, 2009). Heat flow can shape the geometry of the seismogenic zone, wherein high heat flow correlates to thinner seismogenic crust (Bonner et al., 2003). Heat flow can also control the style of earthquake clustering, example, swarm-like earthquakes correlate to regions of high heat flow and burst-like earthquakes to low heat flow regions (Zaliapin & Ben-Zion, 2016a).

3. Data

3.1. Seismic

Data from two seismic arrays (Figure 2) are used to investigate earthquakes in the Raton Basin from July 2016 to July 2020 (Table S1 in Supporting Information S1). The first is an eight-station broadband array with ∼30 km inter-station spacing and continuous 100 Hz sampling. Seven of the stations were deployed in 2016 (Table S1 in Supporting Information S1, UNM1-7). The eighth station, T25A, is a legacy EarthScope Transportable Array station located near the eastern edge of the basin. The second array is composed of 96 Fairfield-Magseis 3-C nodes deployed in the southern portion of the basin from May to June 2018 (Figure 2, Table S1 in Supporting Information S1). The nodes contain 5-Hz geophones. They were spaced ∼2–5 km apart and recorded continuously with a sample rate of 250 Hz.

3.2. Wastewater Injection

Publicly available wastewater injection volume data are used to investigate spatial and temporal changes in injection volume for the Raton Basin. Public injection records are accessible through online databases by state, i.e., the Colorado Oil and Gas Conservation Commission (COGCC, 2021) and the New Mexico Oil Conservation Division (NMOCD, 2021). The monthly injection volume is reported for each well in Colorado (CO) since 1998 (COGCC, 2021) and in New Mexico (NM) since 2006 (NMOCD, 2021). We refer to Rubinstein et al. (2014), who used the produced water volume as a proxy for the injection volume, for estimates of the yearly injection volume in NM prior to June 2006. The number of active wells in the basin varies from 24 to 29 (Figure 2). The current metadata indicates that one well (VPR 007) in NM is located ∼30 km west of the basin (NMOCD, 2021) but we conclude from the permitting documents that the accurate location of this well is ∼200 m northeast of VPR 042. We consider wells located within 250 m of each other to be co-located (Figure 2, two purple squares). When considering injection, data from co-located wells are summed.

4. Methods

4.1. Event Detection and Location

4.1.1. Phase Picking and Association

A deep neural network package called PhaseNet was used to estimate the probabilities of earthquake P and S arrivals within continuous unfiltered seismic data (Zhu & Beroza, 2019). PhaseNet was trained on >600,000 recordings from the Northern California Earthquake Data Center Catalog and has been successfully applied in many regions (e.g., Liu et al., 2020; Park et al., 2020) including the southern portion of the Raton Basin (Wang, Schmandt et al., 2020). Phase detections with a probability ≥0.3 for the broadband array (Figures 3e and 3f) and ≥0.5 for the 1-month node array were passed to the event association step. The 0.3 probability threshold was determined after an analyst visually inspected picks at each station (e.g., Figures 3e and 3f). The average pick probability for the broadband array was 0.86. For the node array, the 0.5 probability follows the threshold set by Wang, Schmandt et al. (2020). Events were associated using the Rapid Earthquake Association and Location algorithm (REAL, Zhang et al., 2019) with the 1-D velocity model from Wang, Schmandt et al. (2020). A minimum of five total phases were required for event association, including at least three P and two S arrivals. Higher thresholds were required during the month of the 96-node array, with ≥50 phases including at least 25 P and 10 S arrivals. A higher probability threshold and a higher requirement for the number of phase picks were set for the nodal seismic data because the primary goal of including this data was to better constrain hypocenters for clusters active during that month rather than to increase the number of earthquake detections. For a focused study on detecting earthquakes during the month of the nodal array see Wang, Schmandt et al. (2020).

We compared the catalog from the automated approach discussed above to a catalog created by the authors using a manual approach. The manual catalog was built using short-term average to long-term average detections (Allen, 1978; Earle & Shearer, 1994) followed by analyst adjustment of P and S picks. There are ∼5,500 earthquakes in the manually refined earthquake catalog from July 2016 to May 2019 and ∼25,000 earthquakes in the automated catalog for the same time period. Comparing >50,000 picks between the automated and manually refined results reveals that 98% of P and 94% of S phase picks are within one tenth

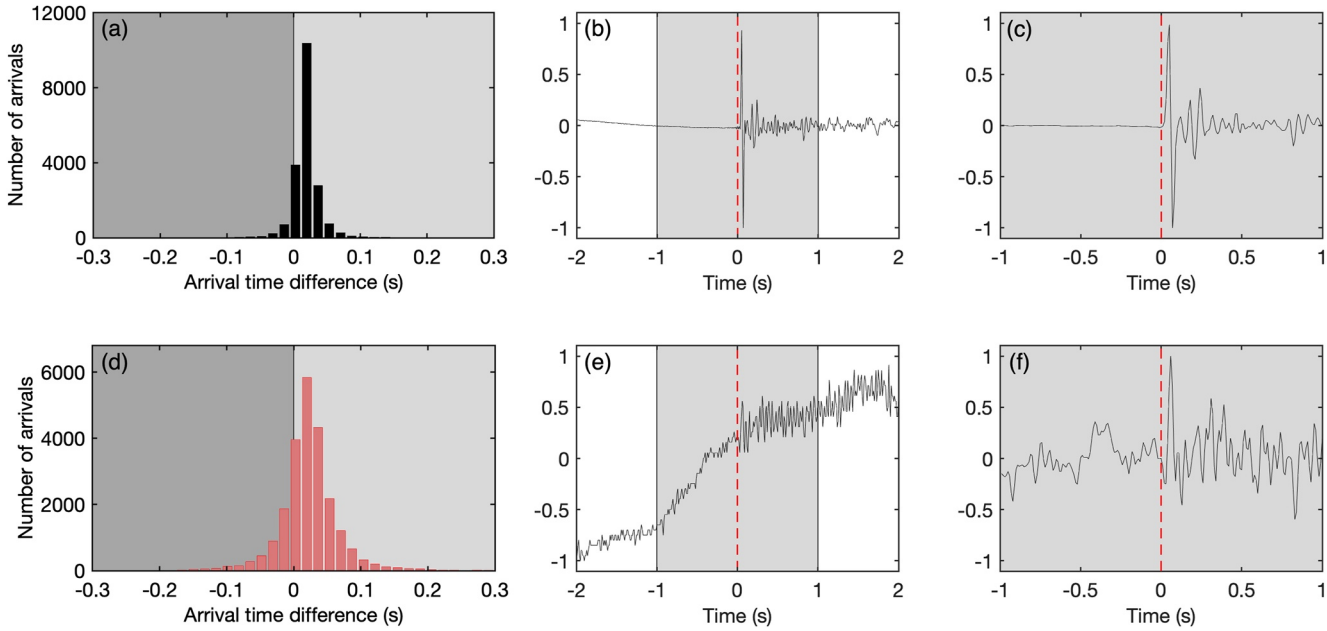

Figure 3. PhaseNet earthquake arrival time results and examples. (a) P and (d) S phase distributions of arrival time differences between manual and automated machine-learning approaches. The dark gray and light gray backgrounds indicate when manual picks are relatively early and late compared to automated machine-learning picks, respectively. (b, c, e and f) Normalized waveforms for events with different probability P arrival (red dashed line) from PhaseNet (Zhu & Beroza, 2019). Panel (b and e) show unfiltered waveforms. Panel (c and f) show zoomed and corresponding waveforms filtered between 1 and 20 Hz. Panel (b and c) high (0.99) and (e and f) low (0.3) probability.

of a second of each other. Manual picks are slightly (0.018 s on average) later relative to the automated machine-learning picks (Figures 3a and 3d). The automated approach results in an ~4.5-fold increase in the number of events detected. Only the catalog built using the automated workflow (PhaseNet, REAL) is considered hereafter.

4.1.2. Hypocenter Estimation

Initial locations from REAL were refined using VELEST, a least squares absolute hypocenter estimation method (Kissling et al., 1994), with the 1-D velocity model from Wang, Schmandt et al. (2020). The earthquake catalog with absolute locations from VELEST includes 37,866 earthquakes from July 2016 to July 2020 (Figures 4a and 4d).

The catalog was relocated using GrowClust (Trugman & Shearer, 2017), which relies on waveform similarity to cluster earthquakes and estimate relative locations with correlation-based differential times. The 1-D velocity from Wang, Schmandt et al. (2020) was used with GrowClust. Prior to cross-correlation, bandpass filtered (1–20 Hz) waveforms were cut from −1 to 1.5 s for P arrivals and −1 to 2.5 s for S arrivals similar to Trugman and Shearer (2017). Each earthquake was correlated with its 300 nearest neighbors in distance. The East or North horizontal channel with the higher correlation was used for S. A range of cluster connectivity ratios and correlation threshold parameters were tested because they affect the spatial compactness and splitting of hypocenter clusters (see Figure S1 in Supporting Information S1 for examples and details). The orientation of earthquake clusters remained fairly consistent between parameter tests (Figure S1 in Supporting Information S1). Only event pairs with cross-correlation coefficients ≥0.5 are considered. For final results, the connectivity ratio was set to 0.01 and a minimum of 5 phases with cross-correlation coefficients ≥0.6 were required (Figures 4b and 4e). Sixty percent (22,684 of 37,866) of the earthquakes were relocated (Figure 4b) and GrowClust identified 91 clusters with >50 earthquakes and 46 clusters with >100 earthquakes. Growclust's nonparametric error estimate was used to estimate the relative location error. Under the presumption that the velocity model is correct, the median horizontal and vertical earthquake location errors are 180 and 240 m, respectively, following 100 bootstrap resamples.

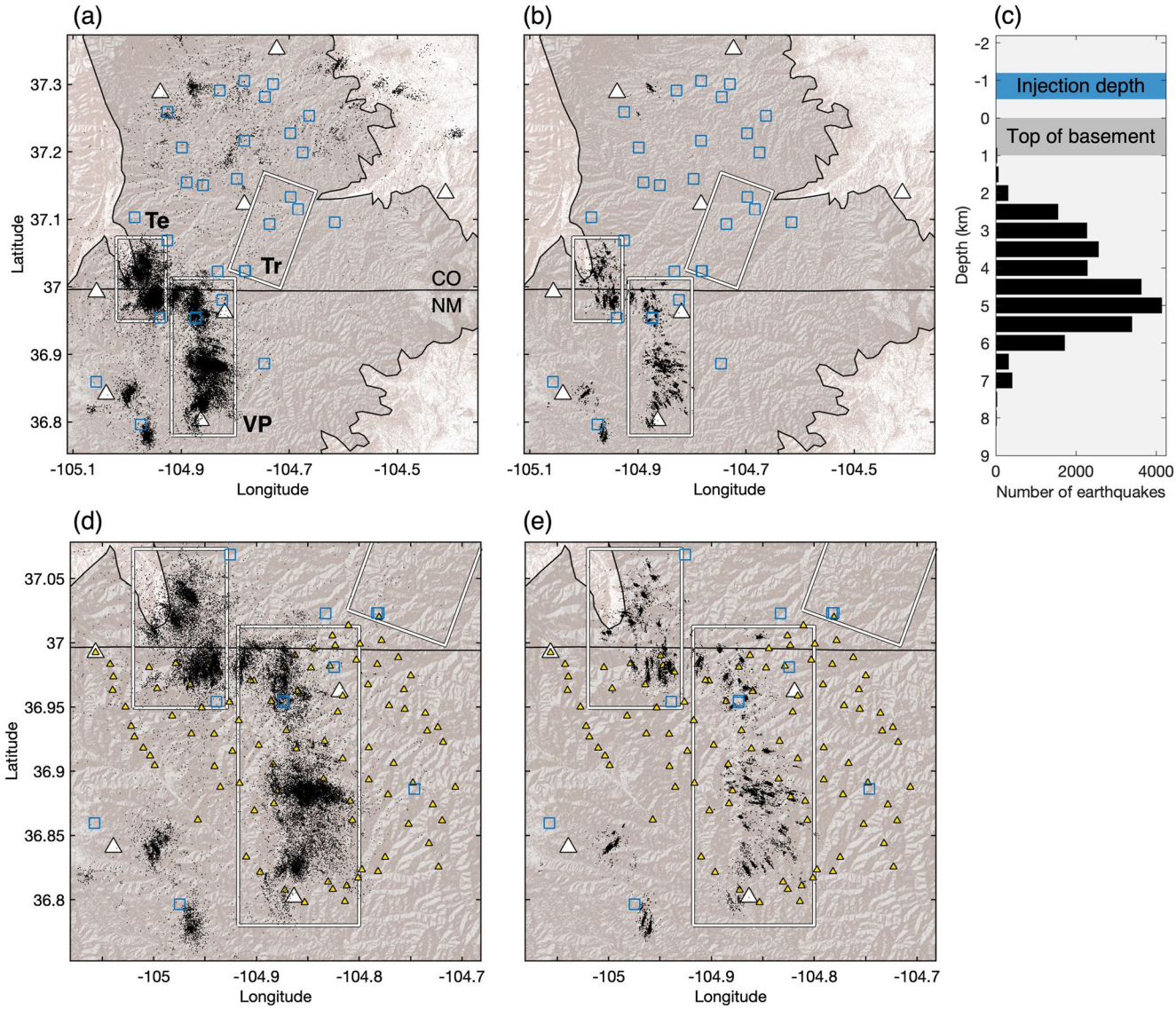

Figure 4. Earthquake locations. The basin is outlined in black. The state border is a black line. The white boxes outline regions of seismicity identified by past studies (Nakai, Weingarten, et al., 2017; Rubinstein et al., 2014). They are abbreviated Te—Tercio, Tr—Trinidad, and VP—Vermejo Park in (a). (a) The absolute locations of the ~38,000 earthquake catalog after VELEST (black dots) and (b) the relative relocations of ~23,000 earthquakes after GrowClust (black dots). (c) The depth distribution of relative relocation earthquakes from (b). Sea level is zero km depth. The depth range of the wastewater injection is shaded in blue. The depth range of the top of the basement is shaded in dark gray. Panel (d and e) zoom in on the most seismically active regions from (a and b) respectively. White triangles are broadband seismometers. Blue squares are wastewater injection wells. Yellow triangles are geophone nodes.

4.2. Local Magnitude Calculation

Three-component waveforms were filtered from 0.01 to 40 Hz, corrected for instrument response, and converted to Wood-Anderson displacement (Uhrhammer & Collins, 1990). Waveforms were cut 0.5 s prior to the P arrival to 3 s after the S arrival for local magnitude (M_L) calculations (Gutenberg & Richter, 1956). To maintain consistency throughout the four-year catalog, only broadband waveforms were considered for magnitude calculation. The maximum three-component vector amplitude (A) in micrometers and the earthquake-station distance (D) in kilometers were used to calculate the local magnitude for each station. The magnitude formula (Gutenberg & Richter, 1956) was calibrated with the 10 largest earthquakes from full waveform moment tensor inversions:

$$M_L = log_{10}(A) + 2.56log_{10}(D) - 4.69$$

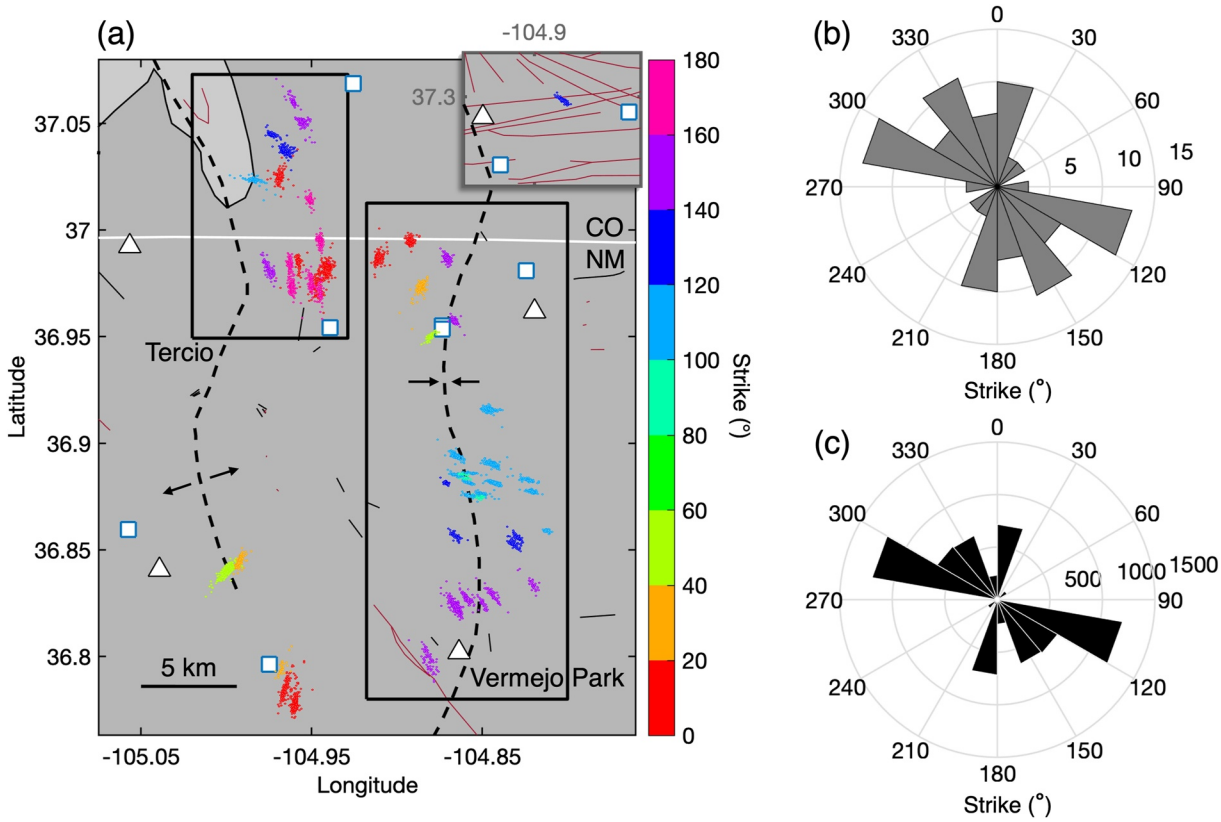

Figure 5. Estimated fault orientations. (a) Dots mark earthquake epicenters and the colors correspond to the estimated strike of the epicenter cluster based on the principal component analysis (PCA). The inset shows the single cluster located outside of the main figure region. Surface geology includes faults (thin black lines), dikes (red lines), synclines and anticlines (black dashed lines). The Tercio and Vermejo Park zones (black boxes) are labeled. Triangles are seismometers and squares are wastewater injection wells active during 2016–2020. The basin has a dark gray background and a black outline. (b) A summary of the strike distribution of the estimated faults from PCA in (a). (c) The distribution of $M_L > 0.5$ earthquakes from (a) by fault strike. The minimum magnitudes of completeness for the Tercio zone and Vermejo Park zones are 0.1 and −0.2, respectively. Panel (b and c) are symmetric, example, the 0–20° bin is equal to the 180–200° bin.

The final estimate is the median of all stations M_L for the event.

4.3. Fault Determination

A two-dimensional principal component analysis (PCA) was used to estimate the strikes of clusters containing 40 earthquakes or more identified by GrowClust. The earthquake-station distance and the small range of earthquake depths (Figure 4c) deter us from using three-dimensional PCA to estimate fault dip. Bootstrap resampling with 100 iterations was used to reduce the effect of potential outliers on the PCA results and estimate strike uncertainties. Only mean strikes with one standard deviation <10° were accepted. In addition, clusters where the first principal component was less than two times greater than the second principal component were rejected. In total, 57 clusters passed the criteria for strike estimation (Figure 5).

4.4. Source Mechanism Constraints

Deviatoric moment tensors were estimated for 27 M ≥ 2.8 earthquakes, which produced low-frequency waveforms suitable for inversion with the Time Domain Seismic Moment Tensor (TDMT) package (Dreger, 2003). The same 1-D velocity model used for hypocenter estimation (Wang, Schmandt et al., 2020) was used to calculate a Green's function library for TDMT inversions. A frequency band of 0.08–0.4 Hz was used, and the window length varied between 10 and 15 s, depending on the source-receiver distance. The parameter choices were adopted from previous studies in a similar setting (e.g., Wang et al., 2016, 2018). Although only eight stations are available, they are all within ~50 km and approximately evenly distributed

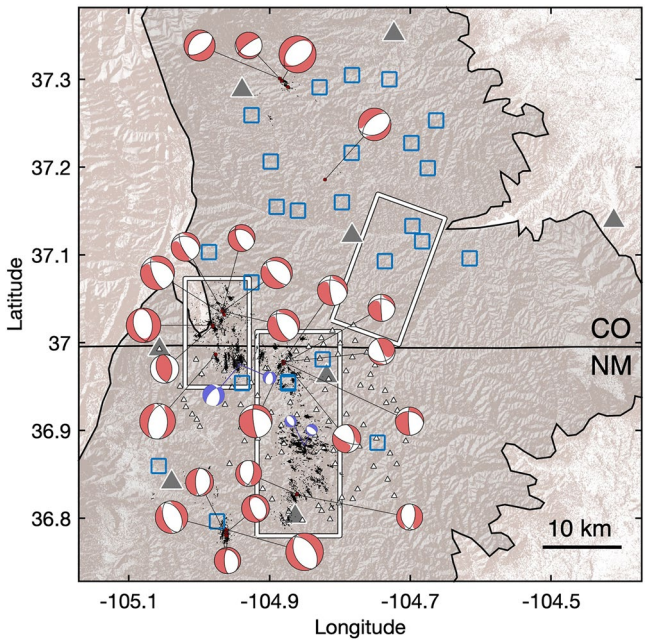

Figure 6. Source mechanism constraints. Deviatoric moment tensor inversion (red and white) resolved from broadband station (gray triangles) recordings. First-motion polarity based focal mechanism inversion results for four smaller magnitude events (purple and white) were resolved using nodal station (small white triangles) recordings. The size of the beachball symbols scales with M_L from 1.26 to 3.99. From east to west, white boxes mark the Trinidad, Vermejo Park, and Tercio zones. Blue squares are the active wastewater injection wells between 2016 and 2020. The apparent inconsistency between the moment tensors and hypocenter cluster near 37.3°N is discussed in Section 5.2.

so azimuthal gaps are limited for events within the Raton Basin. Even the 2 out of 27 events inverted with four stations showed mechanisms comparable to those estimated from larger events nearby. During the fitting of deviatoric moment tensors (i.e., no volumetric component), the average variance reduction for TDMT inversion results is 66% and the highest is 90%. Event epicenters were taken from the newly developed catalog and depths were independently optimized based on a grid-search with 1-km increments. The depths estimated with moment tensor inversions are consistent with the catalog, with a mean difference of 0.26 km (±1.58 km).

Some highly active clusters did not host any M ≥ 2.8 events during the study period and therefore, do not have moment tensor solutions. These clusters were investigated with focal mechanism estimates using first-motion polarities (i.e., FOCMEC; Snoke, 2003). One area targeted for first-motion focal mechanism analysis was the concentration of hypocenter clusters with strikes of ~100° located in the center of the previously identified ~N-S Vermejo Park zone (Figure 5). Additionally, two prominent clusters within the Tercio zone (Figure 5) were investigated. As a result, four additional focal mechanisms are included in Figure 6 (purple beach balls). These events with M_L from 1.26 to 2.33 provided between 70 and 92 clear first-motion polarity picks (Figure S2 in Supporting Information S1).

4.5. Statistical Analysis

The statistical behavior of earthquakes in a region have been used to discriminate between induced and tectonic sequences (e.g., Mousavi et al., 2017; Schoenball et al., 2015; Zaliapin & Ben Zion, 2013, 2016b). A variety of statistical analyses were used to investigate how Raton Basin seismicity is distributed in magnitude, time, and space. Each approach was applied to the full basin and three subregions: the northern basin, the Tercio zone, and the Vermejo Park zone (Figure 7). The additional earthquake detections from using the nodal array were not considered to maintain spatiotemporal and magnitude consistency throughout the catalog. The frequency-magnitude distribution is considered first to estimate magnitude of completeness (M_c) and the slope of the decay in earthquake frequency with increasing magnitude (b-value). M_c and b-value were estimated using the maximum curvature method (Wiemer & Wyss, 2000). We note the maximum curvature method may underestimate M_c by 0.1 (Woessner & Wiemer, 2005). The 95% confidence intervals of b-values were calculated using ZMAP (Reyes & Wiemer, 2020; Wiemer, 2001). A b-value of ~1 is expected given the Gutenberg-Richter law but has been suggested to deviate in regions of high heat flow and/or where fluids are present, including subduction zones, volcanic settings, geothermal fields, and oil and gas fields (Bachmann et al., 2012; Farrell et al., 2009; Goebel et al., 2016; Mousavi et al., 2017; Roberts et al., 2015; van Stiphout et al., 2009). Only earthquakes with magnitudes greater than each region's M_c (Figure 8a) are included in the subsequent statistical assessments (e.g., Figures 8c and 8d).

Spatiotemporal and magnitude clustering of earthquakes were investigated using three approaches: interevent time distributions (Kagan & Jackson, 1991), optimized Epidemic Type Aftershock-Sequence models (ETAS; Harte, 2010; Ogata, 1988), and nearest neighbor space-time distributions (Baiesi & Paczuski, 2004; Schoenball et al., 2015; Zaliapin & Ben-Zion, 2013, 2016b). First, interevent times and the coefficient of variation (C_V) indicate the degree of temporal clustering of earthquakes. The interevent time is the time (in seconds) between events and the C_V is the standard deviation divided by the mean of interevent times. A C_V of one indicates a Poissonian process (e.g., independent or background seismicity), $C_V > 1$ indicates temporal clustering of seismicity (e.g., earthquake-earthquake interactions), and $C_V > 4$ indicates highly clustered earthquakes (Cochran et al., 2018; Kagan & Jackson, 1991; Schoenball & Ellsworth, 2017b). A range in the degree of temporal clustering has been observed for regions of induced seismicity, including

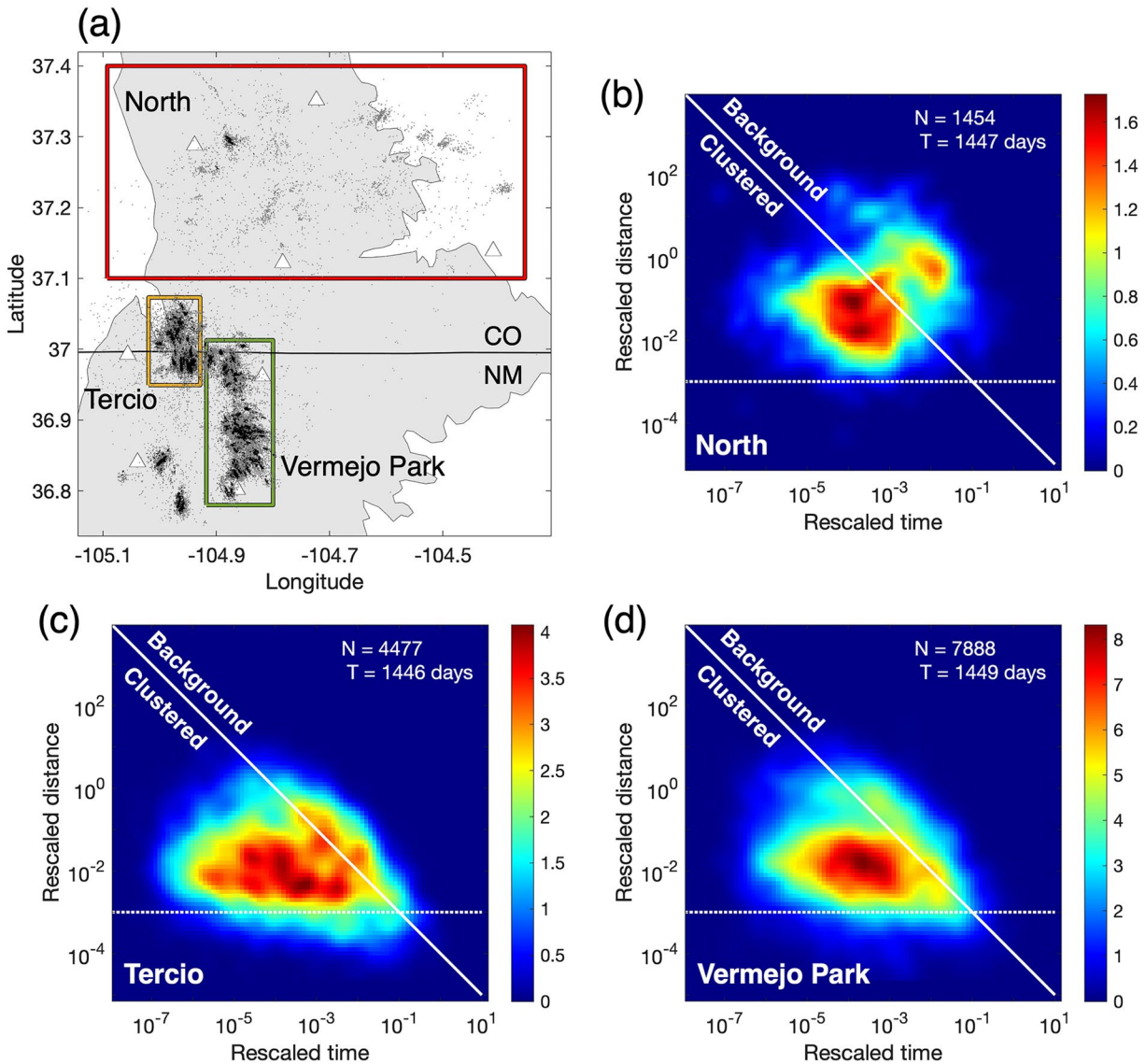

Figure 7. Nearest neighbor time-distance distributions for seismicity in subregions of the Raton Basin. (a) Map of earthquakes and subregions: North subregion outlined in red, Tercio zone outlined in yellow, and Vermejo Park zone outlined in yellow. Absolute epicenters are gray dots and relative epicenters are black dots. Seismometers are white triangles. (b–d) The nearest neighbor distribution results for each subregion. The subregion is labeled in bottom right of each plot. Absolute locations were used for the results shown in (b) and relative relocations for the results in (c and d). The color bar indicates the number of event pairs at a given rescaled distance-time. The number of earthquakes, N, and the time period, T, is printed on each figure. The diagonal white line represents a stationary behavior, wherein rescaled distance ($\boldsymbol{R}_{ij}$) by rescaled time ($\boldsymbol{T}_{ij}$) equals a constant. The horizontal white dotted line represents a constant rescaled distance. Consistent lines are used for all nearest neighbor distance figures for direct comparisons.

near-Poissonian to highly clustered (Cochran et al., 2018; Skoumal et al., 2020) and these temporal behaviors could reflect different processes driving the seismicity. For example, Cochran et al. (2018) observed lower C_Vs from earthquake families close to high-volume injection and suggested these sequences are driven directly by pore fluid pressure increases; in contrast, high-C_V clusters further from wells are highly clustered and imply strong earthquake-earthquake interactions.

The second approach, ETAS modeling, considers event magnitude and time as it predicts the earthquake rate of a stationary Poisson process plus time-decaying aftershocks. We use the ETAS model proposed by Ogata (1988) and updated by Harte (2010) wherein the rate of occurrence of the entire earthquake sequence at time based on the history of occurrence ($Ht = \{(t_i, M_i); t_i < t\}$) is:

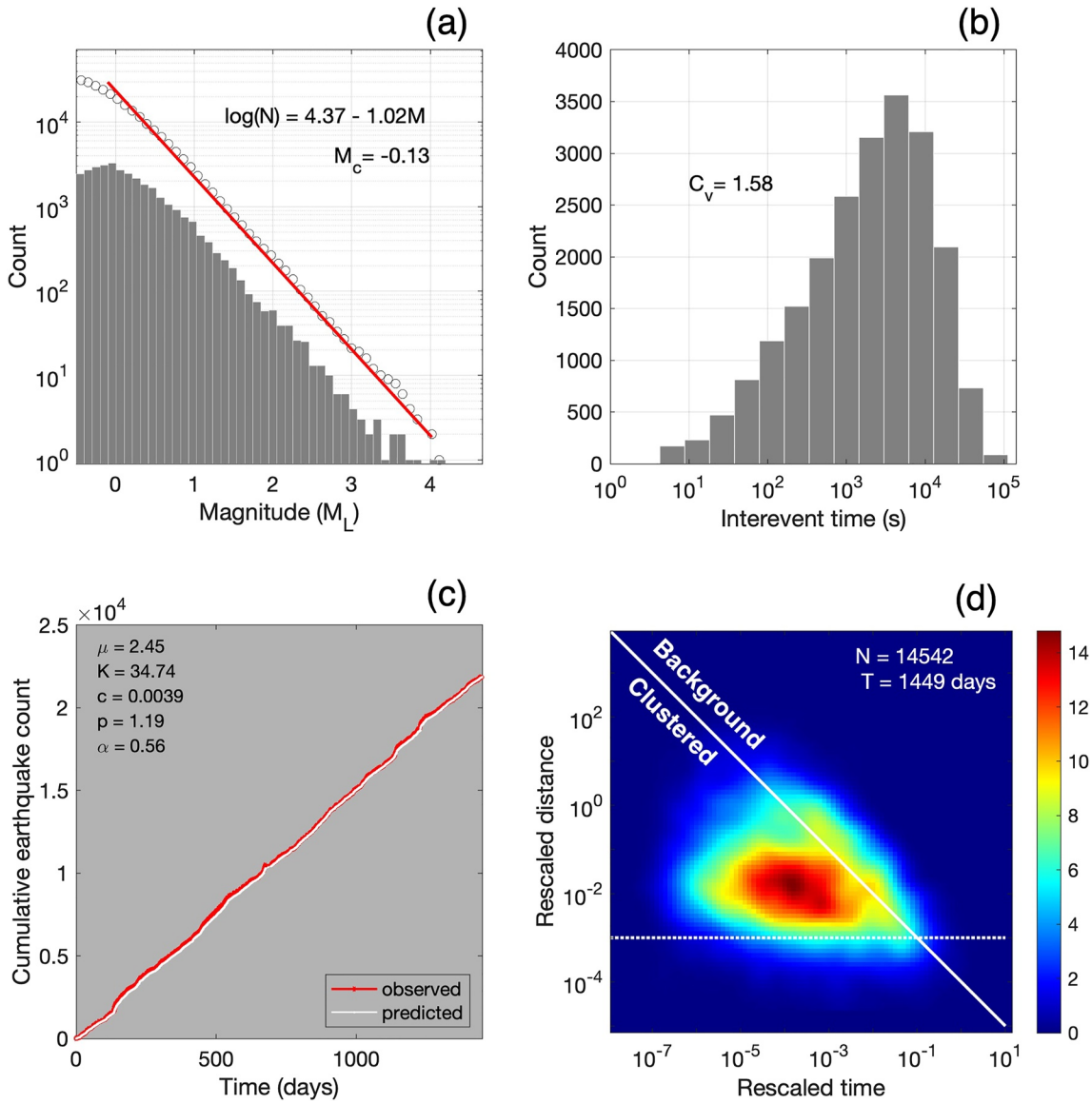

Figure 8. Raton Basin frequency-magnitude and spatiotemporal statistical results. (a) Earthquake frequency-magnitude histogram (gray bars; noncumulative) and cumulative earthquake distribution (gray circles). The red line approximates the best least squares fit to the Gutenberg-Richter relation above the minimum magnitude of completeness (M_c). (b) Interevent time histograms. The average coefficient of interevent time variation (C_v) is printed. (c) Cumulative number of earthquakes versus the number of days from observed seismicity (gray) and Epidemic Type Aftershock-Sequence (ETAS) modeling (black line). ETAS maximum likelihood parameter estimates are printed (Ogata, 1988). (d) Nearest-neighbor rescaled time-distance distribution. The color bar indicates the number of event pairs at a given rescaled distance-time. The diagonal white line represents a stationary behavior, wherein rescaled distance ($\boldsymbol{R_{ij}}$) by rescaled time equals a constant ($\boldsymbol{T_{ij}}$). The horizontal white dotted line represents a constant rescaled distance. Consistent lines are used for all nearest neighbor distance figures for direct comparisons.

$$\lambda(t|Ht) = \mu + K \sum_{i:t_i<t} e^{\alpha(M_i - M_c)} \left(1 + \frac{t - t_i}{c}\right)^{-p}.$$

Here, t_i is the time of the $^{\text{th}}$ event with magnitude M_i and M_c is the magnitude of completeness for each considered region in our study. The parameters, K, c, and p describe the frequency of aftershocks, wherein, K is the aftershock productivity and c and p are the Omori-Utsu parameters for the temporal decay of seismicity following the mainshock (Omori, 1894; Utsu, 1961). The K for this study follows Harte (2010) and is equal to $K_0 c^{-p}$ from the Ogata (1988) study. The parameter α measures the efficiency of an earthquake of a given magnitude to trigger aftershocks (i.e., large α for earthquake swarms which lack typical

aftershock behavior). Lastly, μ is the background seismicity rate (i.e., the forcing rate), which is assumed to be stationary for short time scales but has been found to correlate temporally with injection operations in some induced seismicity settings (e.g., Brodsky & Lajoie, 2013). The ETAS parameters are determined when a minimum tolerance of 0.001 is reached during optimization. Many studies focus on the time-dependent changes of ETAS parameters (Hainzl & Ogata, 2005; Lei et al., 2008) but Llenos and Michael (2013) suggest the absolute values of ETAS parameters could be a way to differentiate between natural earthquakes and anthropogenically induced earthquakes. Induced seismicity may have higher values of K and μ and natural seismicity may have lower values of α (Llenos & Michael, 2013).

Finally, nearest neighbor distance (NND) distributions in the space-time-magnitude domain are indicative of the independent and/or clustered nature of an earthquake sequence or a region's seismicity. We calculate NND in the space-time-magnitude domain (Baiesi & Paczuski, 2004) for each pair of events i and j using the following equation:

$$\eta_{ij} = \begin{cases} t_{ij}\left(r_{ij}\right)^{d} 10^{-bm_i}, & t_{ij} > 0; \\ \infty, & t_{ij} \leq 0, \end{cases}$$

where t_{ij} is the interevent time (year), r_{ij} is the interevent distance (km), d is the dimension of the earthquake hypocenter distribution, b is the b-value, and m_i is the ith event's magnitude (Schoenball et al., 2015; Zaliapin & Ben-Zion, 2013). We set $b = 1$ based on our b-value results discussed in Section 5.3 and we set $d = 1.6$ (Cochran et al., 2020; Vasylkivska & Huerta, 2017; Zaliapin & Ben-Zion, 2013). Both Schoenball et al. (2015) and Zaliapin & Ben-Zion (2013) find the variation of d within 0.5 units of its true value does not significantly affect their results. Following Zaliapin et al. (2008), we can separate the η_{ij} equation into rescaled distance (R_{ij}) and rescaled time (T_{ij}) components where:

$$R_{ij} = \left(r_{ij}\right)^{d} 10^{-bm_i/2},$$

$$T_{ij} = \left(r_{ij}\right)^{d} 10^{-bm_i/2},$$

and

$$\eta_{ij} = R_{ij}T_{ij}.$$

For an ETAS-like earthquake sequence the NND distribution is bimodal with a signal at shorter rescaled distances indicating clustered behavior and a signal at larger rescaled distances indicating independent background behavior (Zaliapin et al., 2008). For NND results in Figures 7 and 8, the relocated earthquake catalog was used except for in the case of the northern basin, where only a small number of events (~280) were accepted for relative relocation (Figure S3d in Supporting Information S1). A comparison between NND results using absolute locations and relative relocations for each region can be found in Figure S6 in Supporting Information S1. A higher ratio of background to clustered seismicity has been found in some induced settings (Cochran et al., 2020; Schoenball et al., 2015; Zaliapin & Ben Zion, 2016b) compared to tectonic settings. Also, the presence of repeaters, earthquakes that occur at short rescaled distances and long rescaled times, are suggested as an induced seismicity signal (Kraft & Deichmann, 2014; Zaliapin & Ben Zion, 2016b). In addition to the type of seismicity (e.g., induced, tectonic), geologic setting is suggested to affect the spatiotemporal-magnitude statistics (Martínez-Garzón et al., 2018; Vasylkivska & Huerta, 2017). We use NND distributions to compare the Raton Basin to regions of tectonic seismicity and other regions of induced seismicity.

5. Results

5.1. Spatial Clustering of Hypocenters

The majority of hypocenters are tightly clustered in geometries consistent with earthquake activity on unmapped basement faults ~2.5–6 km below sea level (Figure 4c). Absolute earthquake locations are heavily concentrated in the central to southern basin with 90% of earthquakes (~34,000) south of 37.05 latitude

(Figure 4a). The absolute earthquake locations (Figures 4a and 4d) collapse into dense elongated clusters after relative relocation (Figures 4b and 4e). Two of the three previously identified fault zones, the Tercio and Vermejo Park zones (Figures 2 and 4), are active during our study period, similar to the 2008–2010 study by Nakai, Weingarten, et al. (2017). Very few earthquakes were detected in the Trinidad zone. Small seismically active zones were identified in the southwest and northwest of the basin by absolute and relocated epicenters (Figures 4a and 4b). One of the southwestern clusters was previously identified by Wang, Schmandt et al. (2020) using only one month of nodal data. Absolute hypocenters are sparsely distributed in the remainder of the northern basin, however all but the northwestern group were culled by the relocation criteria.

Application of a PCA to the relocated earthquake epicenters indicates 57 short (<3 km long) faults (Figure 5a). The majority of the faults (48 out of 57) strike from approximately WNW to slightly east of north (Figure 5b). WNW-ESE striking faults are the most seismogenic, hosting ~33% of the total $M_L \geq 0.5$ earthquakes in Figure 5c.

5.2. Source Mechanism Constraints

Most focal mechanisms from full moment tensor inversion and first motion polarities are consistent with the regional scale normal faulting regime (Lund Snee & Zoback, 2020), with a few exceptions showing oblique or reverse regimes (Figure 6). The strike orientations vary from NE to WNW from north to south. More heterogeneous strikes are observed near the boundary of New Mexico and Colorado (Figures 5 and 6). In general, the strikes estimated from the PCA (Figure 5) and potential fault planes from focal mechanisms (Figure 6) are comparable in the central to southern basin where most seismicity occurs, and the seismograph distribution minimizes azimuthal gaps. Several oblique mechanisms and one reverse faulting mechanism are in the central to southern basin (Figure 6). The reverse event is located in the middle of the Tercio zone. Most other events in the Tercio zone indicate ~NW striking normal faults. Oblique mechanisms are more prevalent near the transition between the Tercio and Vermejo Park zones. Most mechanisms farther south within the middle to southern portion of the Vermejo Park zone indicate WNW to N normal faults (Figures 5 and 6).

A notable example of inconsistency between the moment tensor and the PCA results is found for one fault near the northern edge of the array, ~37.3°N (Figure 6). Its PCA strike estimate is NW, and its moment tensor strike estimate is NE (Figure 5a inset & Figure 6). The different strikes of the PCA and moment tensor analysis could be explained by the activation of non-optimally oriented faults through large pressure perturbations, tens of MPa, as has been suggested for the 2014 M_W 4.9 Milan, Kansas earthquake (Joubert et al., 2020). However, given the location near the edge of the array the epicenters may be biased by limited azimuthal coverage in which case the PCA strikes could be incorrect. The three-component waveform-based moment tensor estimate of strike is preferred in this location. Additionally, maximum compressive stress indicators near 37.3°N show orientations of ~NNE-NE (Figure 2; Lund Snee & Zoback, 2020), which would be consistent with a ~NE striking normal fault.

5.3. Frequency, Magnitude, and Temporal Clustering Statistics

Space-time-magnitude statistics are calculated for the full basin and three subregions: the northern basin, the Tercio zone, and the Vermejo Park zone (Figures 7 and 8; Figures S3–S6 in Supporting Information S1). The M_c varies spatially due to station coverage (Figures S3–S5 in Supporting Information S1). Although $M_c = -0.13$ for the entire catalog (Figure 8a), we conservatively suggest that the catalog is complete to ~M_L 0.6 since this was the maximum M_c of the subregions (Figures S3–S5 in Supporting Information S1). However, the following statistical results were all derived using earthquakes with M_c unique to each considered region. The maximum magnitude during our study is M_L 4.2. The b-value for the entire study region is 1.03 (Figure 8a) and its 95% confidence interval (CI) is 0.95–1.09. The b-values of the three subregions are 1.07 (0.57–1.58 95% CI) for the north, 0.98 (0.90–1.07 95% CI) for the Tercio zone, and 1.05 (1.047–1.054 95% CI) for the Vermejo Park zone (Figures S3a–S5a in Supporting Information S1).

Interevent times range from ~10^1 to 10^5 s and the full basin C_v is ~1.6 (Figure 8b) indicating low to moderate temporal clustering of the seismicity. The C_v of each subregion is slightly higher than the full basin, ~1.8

for Vermejo Park, ~1.9 for Tercio, and ~2 for the north (Figures S3b–S5b in Supporting Information S1). The C_v values for induced earthquakes in Oklahoma and southern Kansas range from ~1 to 10 (Cochran et al., 2018; Schoenball et al., 2018) implying a variety of temporal clustering from little or none to highly clustered. We find a narrower range of results with C_v values from ~1.6 to 2 indicating low to moderate temporal clustering and no significant variation between regions at the temporal and spatial scale considered.

ETAS modeling visually fits the observed seismic rate for the full basin (Figure 8c), as well as the Tercio and Vermejo Park regions (Figures S4c and S5c in Supporting Information S1). This demonstrates that most of the observed seismicity in the Raton Basin can be modeled by time-independent events and subsequent aftershocks. A minor exception is that for the northern subregion, ETAS often underpredicts the seismic rate (Figure S3c in Supporting Information S1) indicating the observed rate has even higher productivity of earthquake-earthquake interactions than predicted by ETAS. The decay parameters (c and p) are comparable between the subregions and consistent α were observed across the multiple subregions, indicating similar magnitude productivity (Figures S3c–S5c in Supporting Information S1). The productivity values (K as defined by Harte, 2010) for the southern sections, ~32–40, are orders higher than that of the northern section (4), echoing differences in the number of events observed during the same four-year period. The full-basin statistics, as a result, are dominated by the southern sections (i.e., Tercio and Vermejo Park), characterized by steady seismicity rate over the four years studied. Although there are variations in the injection volume and rate in each considered subregion (Figure S7 in Supporting Information S1), we did not observe significant differences in the μ parameters, which often reflect the forcing rate from external contribution (e.g., Llenos & Michael, 2013, 2016; Kothari et al., 2020). The invariance of μ with injection strategies (and the other four parameters), however, does not imply the natural origin of the seismicity, but rather implies a complex (i.e., non-linear) and delayed response between the injection activities and earthquake rates and/or that the tectonic forcing is more dominant than the forcing from fluid injection.

NND distributions for the full basin (Figure 8d) are slightly bimodal with the largest concentration of event pairs at short space-time distances corresponding to clustered seismicity and a smaller distribution along a constant slope corresponding to independent background seismicity. NND distributions for the three subregions (Figures 7c and 7d) also exhibit a strong clustered behavior and comparatively weak independent behavior. The dominance of the clustered mode at 10^{-2} rescaled distance and 10^{-4} rescaled time in Figure 8d is similar to the results for the induced setting of southern Kansas and Oklahoma (Schoenball & Ellsworth, 2017b; Verdecchia et al., 2021) and the mixed (induced and tectonic) setting of the Salton Sea geothermal area (Zaliapin & Ben Zion, 2016b). But our results are dissimilar from some induced seismicity settings where strong ratios of background to clustered signals have been identified (Cochran et al., 2020; Schoenball et al., 2015; Zaliapin & Ben Zion, 2016b). The northern region (Figure 7b) exhibits the clearest separation between the clustered and background mode. However, poorly constrained absolute locations can lead to artifacts at large rescaled space-time distances (Zaliapin & Ben-Zion, 2015). The Vermejo Park zone exhibits the highest ratio of clustered to background signal and its NND pattern dominates the full basin NND distribution (Figures 7d and 8d). A repeater signal may be present for the Vermejo Park zone appearing as a lobe in the bottom right of Figure 7d, but it is not apparent for the other considered regions (Figures 7b, 7c and 8d).

6. Discussion

6.1. Basement Fault Systems Beneath the Raton Basin

The spatial distribution of seismicity in the new catalog provides evidence for local variability of fault orientations that is not apparent in prior work using the EarthScope Transportable Array (Nakai, Weingarten, et al., 2017) or short-term aftershock deployments (Barnhart et al., 2014; Rubinstein et al., 2014). Prior work indicated primarily N to NNE striking normal faulting earthquakes (Barnhart et al., 2014; Nakai, Weingarten, et al., 2017; Rubinstein et al., 2014), which were grouped into three zones of seismicity ~10–20 km in length: the Trinidad, Vermejo Park, and Tercio zones (Figure 2). During 2016–2020, the Vermejo Park and Tercio zones were much more active than the Trinidad zone, whose activity has greatly diminished since hosting a M_W 5.3 event in 2011 and continued to diminish from 2016 to 2020 (Figure 9e). Primarily using EarthScope Transportable Array data with ~70-km station spacing, Nakai, Weingarten, et al. (2017) suggested that the Vermejo Park and Tercio zones were long (~10–20 km) N-S normal faults. With the

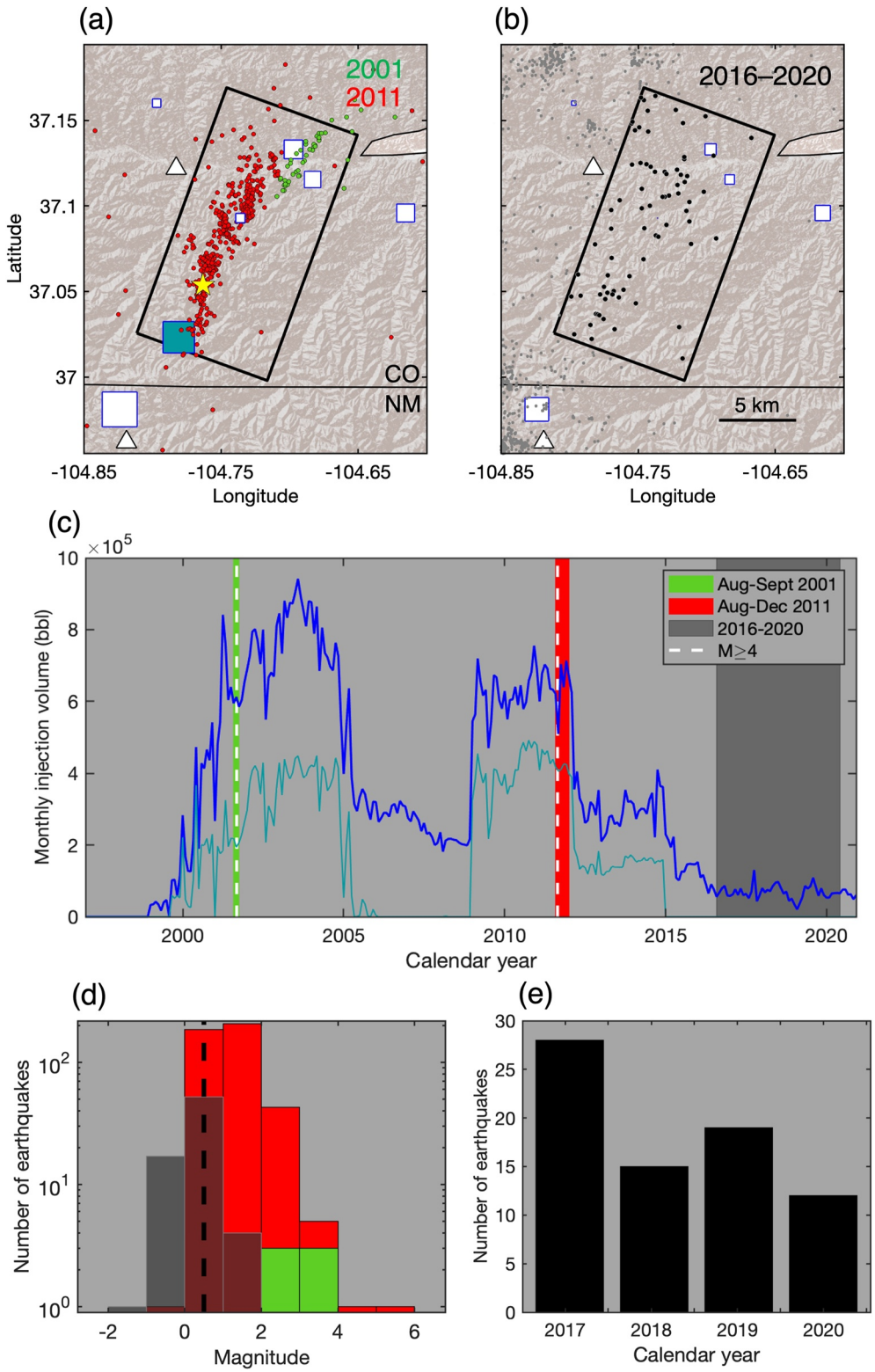
(a)
2001
2011
37.15
37.1
37.05
37
Latitude
CO
NM
-104.85
-104.75
-104.65
Longitude
(b)
2016–2020
5 km
-104.85
-104.75
-104.65
Longitude
(c)
×10^5
10
8
6
4
2
0
Monthly injection volume (bbl)
Aug-Sept 2001
Aug-Dec 2011
2016-2020
M≥4
2000
2005
2010
2015
2020
Calendar year
(d)
10^2
10^1
10^0
Number of earthquakes
-2
0
2
4
6
Magnitude
(e)
30
25
20
15
10
5
0
Number of earthquakes
2017
2018
2019
2020
Calendar year

Figure 9.

local array catalog from 2016 to 2020, we find 57 shorter faults across the Raton Basin with variable strikes (Figure 5) and faulting regimes (Figure 6). Most of these short faults are concentrated in the Vermejo Park and Tercio zones, where discrete faults with lengths of ~1–3 km combine to form the previously identified broader zones of seismicity. The nearly contiguous seismicity between the Tercio and Vermejo Park zones suggests their activity may be linked. These multi-scale fault zone structures are similar to but more extensive than earlier suggestions of en echelon faults within the Trinidad zone near the time of the 2011 M_W 5.3 earthquake sequence (Rubinstein et al., 2014).

A potential implication of the multi-scale fault zone structure is that the maximum potential earthquake magnitude may be smaller if there are no continuous faults that span the ~20 km long Vermejo Park zone or ~10 km long Tercio zone. However, ruptures may span multiple nearby fault segments (e.g., Landers earthquake, Li et al., 1994; and Hector Mine earthquake, Treiman et al., 2002) such that the maximum fault length is not a reliable predictor of the maximum earthquake magnitude. Such co-slipping of en-echelon fault systems has been observed for induced seismicity in Alberta, Canada (M_W 4.1, Wang et al., 2018) and east Texas (M 4.8, Wang, Ellsworth et al., 2020). Within the Raton Basin, the largest earthquake since the beginning of injection was the M_W 5.3 Trinidad event with a geodetically estimated rupture length of ~8–10 km (Barnhart et al., 2014), which is shorter than the ~14 km total length of the Trinidad zone of seismicity (Meremonte et al., 2002; Rubinstein et al., 2014). A local seismic network was not in place prior to the M_W 5.3 event therefore it is unclear whether it ruptured one fault or multiple shorter faults, but the aftershock locations suggest the presence of multiple segments with strikes rotated closer to North, instead of the orientation of the composite Trinidad zone of seismicity (Figure 9a; Rubinstein et al., 2014).

The changes in fault orientation (Figure 5) and evidence of different slip regimes (Figure 6), specifically along the CO-NM border, indicate either stress conditions that change over short-length scales (~5–10 km) or stress perturbations that are sufficient to reactivate non-optimally oriented faults. A stress rotation from N to S maximum horizontal stress in the mid to northern basin to E-W at the southeastern edge (Figure 2) may help explain the variable strikes (Lund Snee & Zoback, 2020; Wang, Schmandt et al., 2020) but there are no stress measurements for comparison in the most seismically active parts of the central to southern basin. Alternatively, the regional stress field may be modified by local stresses or earthquakes may occur on non-optimally oriented faults, as observed in some areas of fluid injection. Such stress perturbations are often observed from high-rate injections like hydraulic fracturing (e.g., Shen et al., 2021) or geothermal exploitations (e.g., Martínez-Garzón et al., 2016). At maximum injection pressures for the Geysers geothermal field, a range of fault orientations are activated including non-optimally oriented faults at maximum injection pressure (Martínez-Garzón et al., 2016). We generally observe more variable fault orientations closer to wastewater injection wells (e.g., the CO-NM border, Figure 5a). Non-optimally oriented faults in Oklahoma and Kansas are suggested to reactivate from either high pore pressure increase or potentially static stress changes from nearby seismogenic faults (Joubert et al., 2020; Sumy et al., 2014). A systematic investigation of fault orientations, injection rates, and static stress changes would provide further insights into the driving mechanism(s) of the induced seismicity.

6.2. Evolution of Wastewater Injection and Seismicity

6.2.1. Full Basin Summary

The seismogenic faults from this study are located in the basement similar to previous studies of Raton Basin seismicity (Nakai, Weingarten, et al., 2017; Rubinstein et al., 2014) as well as Oklahoma and Kansas (Schoenball & Ellsworth, 2017a). Permeable pathways, such as faults, provide a potential link between

Figure 9. Evolution of Trinidad zone seismicity. (a and b) Maps of earthquakes in the Trinidad zone (black box) from (a) August–December2001 (green, Meremonte et al., 2002), August–December2011 (red; Rubinstein et al., 2014) and (b) our July 2016–July 2020 catalog (black and gray). Seismometers are white triangles. Wastewater injection wells are squares and are scaled by average injection volume from 2008 to 2012 for (a) and from 2016 to 2020 for (b). The yellow star is the 2011 M_w 5.3 earthquake epicenter. (c) The total monthly wastewater injection volume within the Trinidad zone is shown in dark blue. The turquoise monthly wastewater injection volume is for two co-located wells shown as a turquoise well in (a). Shaded regions indicate times of earthquake studies, see legend. White dashed lines are M ≥ 4 earthquakes from the USGS catalog within 10 km of the Trinidad zone. (d) Earthquake magnitudes for each catalog within the Trinidad zone. Legend colors from (c) apply to (d). Black dashed line marks the minimum magnitude of completeness for our 2016–2020 catalog. (e) Number of earthquakes per year within the Trinidad zone for our catalog shown in (b).

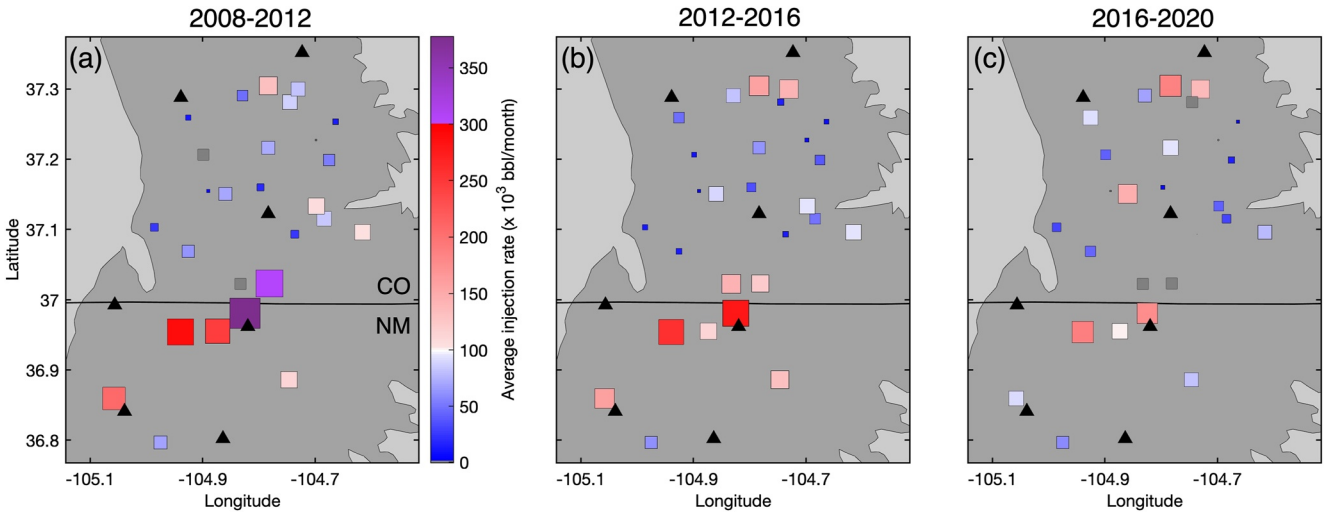

Figure 10. The average monthly wastewater injection volume during three time periods indicated by the titles for (a–c). The color bar from (a) can be used for (b and c). Purple indicates high-rate (>300,000 bbl/month), red indicates moderate-rate (100,000–300,0000 bbl/month), and blue indicates low-rate injection wells (<100,000 bbl/month). Squares scale with the average injection volume and are consistent between figures. Gray squares indicate wells with no reported injection volume. Black triangles are seismometers. The Raton Basin is outlined in black.

shallow wastewater injection and reactivated basement faults under the Raton Basin (Nakai, Weingarten, et al., 2017). In the Raton Basin mapped faults and intrusions are observed at the surface and basement faults are inferred from earthquake locations but there are no direct observations of permeable pathways that connect the injection reservoir to the basement. However, mantle-derived helium often found in geothermal springs along faults at locations near the Raton Basin, example, Sheep Mountain and Bravo Dome, suggests that permeable connections between mantle depths and Earth's surface are common in this region of the southern Rocky Mountains (Karlstrom et al., 2013). Additionally, Hemborg (1998) alludes to higher productivity of coal bed methane beds closer to faults in the Spanish Peak field wells suggesting the potential for enhanced permeability within the basin sediments.

To understand the evolution of wastewater injection, we examine the average monthly injection for three four-year time periods in the Raton Basin (Figure 10). The wastewater injection record by well is complete from 2006 to 2020. Similar to Weingarten et al., (2015), we consider injection ≥300,000 bbl/month as high-rate, <100,000 bbl/month as low-rate, and rates between as moderate. The total injection volume in the Raton Basin for the considered time periods decreases chronologically from 2008 to 2020 (Figures 10a–10c). The number of high-rate injection wells decreased from two during 2008–2012 to zero from 2012 to 2020 (Figure 10). Injection rate declined in the south and central basin from 2008 to 2020 and is more evenly distributed across the basin by 2016–2020 (Figure 10). The northernmost well and two wells just south of the state border remain moderate- to high-rate injectors during all considered time periods. During our earthquake catalog from 2016 to 2020, these three wells operate at >170,000 bbl/month and in total six wells are moderate-rate injectors. Similar injection rates, >150,000 bbl/month, were reported for all wells associated with induced seismicity for the Barnett Shale in Texas but some wells operated at this rate with no associated seismicity (Frohlich, 2012).

Greater than 90% of earthquakes occur less than 10 km from the nearest wastewater disposal well from 2016 to 2020 (Figure 11) with an average earthquake to well distance of 5.8 km. Given the proximity of seismicity to injection wells, pore fluid pressure increases are a likely driver of fault reactivation, but it is not certain how pore fluid pressures are transmitted to basement depths. Although our earthquake depths taper off near the top of the basement (Figure 4c), it is likely permeable conduits, such as faults, extend upward from the basement into the basin sediments. Previous pore fluid pressure modeling along a permeable fault in the Vermejo Park zone indicated increases of 0.08 MPa would be sufficient for triggering earthquakes (Nakai, Weingarten, et al., 2017). Poroelasticity has been found to favor slip for high-angle normal faults beneath the injection reservoir (Chang & Segall, 2016) and may amplify stresses inducing earthquakes in the Raton Basin.

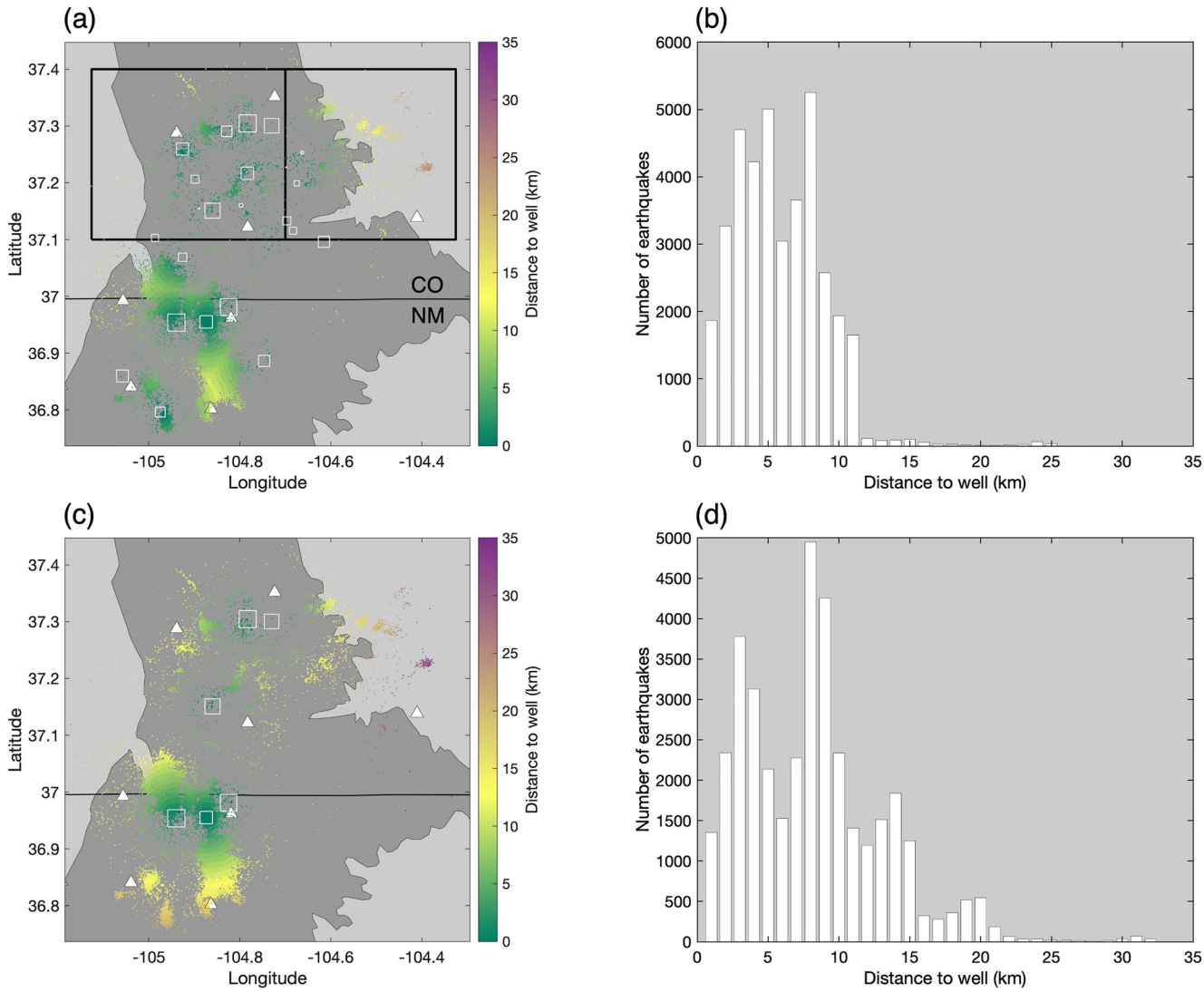

Figure 11. Earthquake distance to nearest wastewater injection well. Map of earthquake distance to (a) the nearest wastewater injection well and (c) the nearest moderate-rate (100,000–300,0000 bbl/month) injection well. Color corresponds to distance. The size of white squares scale with the average monthly injection volume from 2016 to 2020. White triangles are seismometers. The perimeter of the black box in (a) distinguishes the north mentioned in 6.2.3 and the line dividing the box separates the northeast and the northwest. (b) Distribution of distances from (a). (d) Distribution of distances from (c).

The timing of pore fluid pressure changes is strongly dependent on hydraulic diffusivity (Barbour et al., 2017), which may explain the lack of a short-term (<years) temporal correlation between wastewater injection and seismicity (Figure 1a; Figure S7 in Supporting Information S1). The summed injection rate was steady to slightly decreasing from 2016 to 2020 and no apparent correlation exists between the injection rate and earthquake rate (Figure S7 in Supporting Information S1). The temporal evolution in the Raton Basin is similar to other areas where induced seismicity can lag several years behind the initiation of wastewater disposal (Schoenball et al., 2018). The rate of wastewater injection in the basin plateaued from ~2004 to 2014 with an average total of ~2.45 Mbbl/month (Figure 1b). Comparatively, the injection rate has declined 32% in the last 5 years (2016–2021) with an average total of ~1.67 Mbbl/month. The earthquake rate for the same time periods has decreased ~40% (from ~8.5 to 5 $M \geq 3$ earthquakes/year when comparing 2004–2014 to 2016–2021, respectively) which suggests the wastewater injection and seismic record may be correlated when longer timescales (~5–10 years) are considered. Following a rate reduction in wastewater injection, Dempsey and Riffault (2019) suggest induced seismicity will initially decline, experience occasional quiescence, and eventually reach a new equilibrium. The most recent decrease in the earthquake rate

(~1.7 M ≥ 3 earthquakes/year from January 2020 to September 2021, ANSS ComCat, 2021) may reflect an adjustment of the seismicity in response to the reduced wastewater injection rate.

6.2.2. Tercio and Vermejo Park Zones

From 2008 to 2020, the wells with the highest injection rates and largest cumulative injection volume lie within the Tercio and Vermejo Park zones just south of the CO-NM border (Figure 10). These zones are the most seismically active during this study (Figure 11). Two additional wells (VPR 007 and VPR 042) are co-located between the large injectors. All four wells are within ~10 km horizontal distance and <250 m vertical distance of each other. They collectively inject >450,000 bbl/month on average from 2016 to 2020. Weingarten et al. (2015) found the likelihood that a wastewater injection well is associated with earthquakes increases as the maximum injection rate increases, example, high-rate wells (>300,000 bbl/month) are twice as likely to be associated with earthquakes as low-rate wells (<100,000 bbl/month). High-rate wells perturb pressure at larger magnitude and further extent than low-rate wells (Weingarten et al., 2015). The larger spatial effect of high-rate wells also increases the probability of encountering faults. Absolute earthquake locations extend from the area of large cumulative injection along the border to 15 km north in the Tercio zone and 20 km south in the Vermejo Park zone (Figure 11c). At the furthest extents in these zones, earthquakes are closer to other injection wells but are not spatially contiguous with these low-rate wells.

6.2.3. Northeastern Basin

Seismicity is observed at the greatest distance from wells beyond the northeastern margin of the basin. Earthquakes occur up to ~27 km from the nearest injection well and ~35 km from the nearest moderate-rate well (Figure 11). Above basement injection, as is the case in the Raton Basin, has been linked to larger spatial footprints of seismicity in a global compilation (Goebel & Brodsky, 2018). Induced earthquakes have occurred 20–40 km from injection wells in Oklahoma (Goebel et al., 2017; Keranen et al., 2014) and ~25–90 km from high volume wells in Kansas (Ansari et al., 2019; Peterie et al., 2018). Assessing the origin of the more distant events in the Raton Basin is difficult because catalog sensitivity to M < 3 earthquakes is sporadic over the past two decades. The earthquake catalog by Nakai, Weingarten, et al. (2017) from 2008 to 2010, has 70 earthquakes per year in the north and 23 in the northeast above their M_c of 1.3 (see Figure 11a for definition of north and northeast). Using the same M_c, we find a comparable number of earthquakes in the north, 63 earthquakes/year, and 60 percent more earthquakes in the northeast, 37 earthquakes/year. Injection rates in the northern basin have not changed dramatically over time (Figure 10). After two decades of wastewater injection, it is plausible pore-pressure has diffused to the region of northeast seismicity, however, poroelastic effects could be more influential in triggering earthquakes at large distances from wells (Goebel et al., 2017) or on hydraulically isolated faults (Chang & Segall, 2016). Reanalysis of earlier seismic data and further hydrogeologic modeling (e.g., Nakai, Weingarten, et al., 2017) are needed to test potential linkages between the northeastern extent of earthquake activity and wastewater injection at distances >25 km.

6.2.4. Trinidad Zone

Few earthquakes are observed in the Trinidad zone which hosted the largest recorded earthquake in the basin (M_W 5.3) in the second of two short-lived earthquake sequences in 2001 and 2011 (Figure 9, Barnhart et al., 2014; Meremonte et al., 2002; Rubinstein et al., 2014). Approximately 70 earthquakes with $M_L < 2$ are located in the Trinidad zone during our study (Figure 9b) with none surviving the relocation step (Figure 4b). Only one earthquake was located in the Trinidad zone for the 2008–2010 earthquake catalog with $M_c = 1.3$ by Nakai, Weingarten, et al. (2017). The combination of results demonstrates seismicity in the Trinidad zone has included quick bursts of activity and quiescent periods on the order of years.

The monthly injection rate in the Trinidad zone for the years preceding the 2011 sequence was ~600,000 bbl/month (Figure 9c), ~70–80% of which was contributed by the two co-located high-rate wells nearest the M_W 5.3 earthquake (Figures 9a and 9c). In 2012 the injection rate dropped to ~300,000 bbl/month and by 2016 to ~100,000 bbl/month. The two co-located wells were completely shut-in by January 2015, ~20 months prior to our study (Figure 9c). Goebel et al. (2019) found fluid pressures can decrease within the injection reservoir at kilometer-length scales within days of well shut-in. We suggest that the 2011 earthquake sequence depleted the stored tectonic strain in the crust. Furthermore, the Trinidad zone experienced a significant decrease in wastewater injection after 2011, contributing to our observation of a low and declining

seismicity rate from 2016 to 2020 (Figure 9). The Trinidad zone may be a useful example for further studying the evolution of seismicity following cessation of about a decade of injection during which moderate magnitude events occurred.

6.3. Statistical Similarity to Tectonic Sequences

Induced and tectonic settings are expected to have different spatiotemporal-magnitude and frequency-magnitude statistics if the physical mechanisms driving the processes are different. For example, hydraulic fracturing and enhanced geothermal system regions (Mousavi et al., 2017), may have higher b-values than tectonic settings, whereas lower b-values are observed for water-injection-related sequences in the Sichuan Basin (Lei et al., 2019). However, the b-value for the Raton Basin is ∼1, comparable to tectonic settings as well as some other wastewater injection induced seismicity cases in the United States (e.g., Cochran et al., 2020; Mousavi et al., 2017). The b-value of ∼1 suggests that the stress condition that drives seismicity in the Raton Basin is similar to tectonic settings and dissimilar to other induced regions with abnormal b-values.

In cases of clear anthropogenic forcing, such as geothermal stimulation, independent background earthquakes dominate the spatiotemporal-magnitude behavior (Martínez-Garzón et al., 2018; Schoenball et al., 2015). In regions of tectonic earthquakes, fewer independent and more clustered earthquakes are observed compared to some induced settings (Zaliapin & Ben Zion, 2016b). The range of C_v (∼1.6–2) for the full basin and subregions suggests low to moderate temporal clustering. Predictions from ETAS modeling demonstrate the earthquake rate for the full basin, Tercio zone, and Vermejo Park zone can be modeled by time-independent events and subsequent aftershocks. Lastly, the NND distributions (Figures 7 and 8d) reveal a higher ratio of clustered to background seismicity in the space-time-magnitude domain for all considered regions.

The strong clustered behavior of the Raton Basin suggests earthquake-earthquake interactions are more significant than direct forcing by fluid injection, which produces more background events. A study by Schoenball et al. (2018) with similar clustering results to ours led to the conclusion that earthquake sequences in Oklahoma and southern Kansas are initiated by anthropogenic stressing but stored tectonic energy drives sequences. Alternatively, a one-month study by Cochran et al. (2020) found independent sequences dominate Oklahoma seismicity and suggests they are directly driven by the high stressing rates of wastewater disposal wells. Wastewater injection rates in their study region were 7 and 8 Mbbl/month, ∼4 and 5 times the wastewater injection rate during our study (Figure 1b). For the Raton Basin we suggest, similar to Schoenball et al. (2018), that small changes in pore fluid pressure from moderate- to low-rate wastewater injection decreases the frictional resistance on faults, permitting the stored tectonic stress to initiate slip and continue through interevent triggering (earthquake-earthquake interactions).

7. Conclusions

A four-year earthquake catalog of ∼38,000 earthquakes improves the resolution of the seismogenic structures in the Raton Basin and provides us the opportunity to characterize the earthquake behavior through spatiotemporal-magnitude statistical analyses. Sixty short, 1–3 km long, faults with a range of strikes from WNW to NNE are active in the basement beneath the Raton Basin. The majority of fault motion agrees with the regional scale normal faulting regime although some oblique and reverse slip exists. High permeable conduits, such as fault zones, likely extend upward from the basement into the basin sediments providing hydraulic connectivity between the injection reservoir and the seismically active faults.

The Tercio and Vermejo Park zones host over 80% of the basin's seismicity. The Trinidad zone that hosted the 2011 M_w 5.3 earthquake experienced low rates of seismicity from 2016 to 2020, likely due to the combined effects of near-complete release of tectonic strain and the large decrease in the wastewater injection rate from 2011 to 2016.

Unlike some regions of induced seismicity with distinct independent background events resulting from direct forcing by fluid injection, the spatiotemporal-magnitude behavior of the seismicity in the Raton Basin is more strongly clustered, similar to tectonic regions. We suggest that the low- to moderate-rate wastewater

injection of the Raton Basin may only initiate earthquake sequences by decreasing the frictional resistance on faults whereas stored tectonic stress is responsible for subsequent earthquake-earthquake interactions.

Conflict of Interest

The authors declare no conflict of interest relevant to this study.

Data Availability Statement

Waveform data and metadata used in this study are publicly available through the Incorporated Research Institutions for Seismology Data Management Center (IRIS DMC) using the network and station information in Table S1 in Supporting Information S1 (http://ds.iris.edu/ds/nodes/dmc/) which include the TA (https://doi.org/10.7914/SN/TA), C0 (https://doi.org/10.7914/SN/C0), YX (https://doi.org/10.7914/SN/YX_2016), and 4E (https://doi.org/10.7914/SN/4E_2018) networks. The Raton Basin earthquake catalog from 2016 to 2020 is available at the International Seismological Centre (https://doi.org/10.31905/127XP53R) and the earthquake phase arrivals are available at Zenodo (http://doi.org/10.5281/zenodo.5579804). Wastewater injection well data for Las Animas County, Colorado was retrieved from (COGCC, 2021; http://cogcc.state.co.us/data.html#/cogis) by opening the "Facility" page and using facility type "WELL", county "Las Animas" and facility status "IJ - INJECTING". Wastewater injection well data for Colfax County, New Mexico was retrieved from (NMOCD, 2021; https://wwwapps.emnrd.state.nm.us/ocd/ocdpermitting/Data/WellSearchResults.aspx?OperatorSearchClause=BeginsWith&WellSearchClause=BeginsWith&WellNumberSearchClause=BeginsWith&PoolSearchClause=BeginsWith&api_cnty_cde=Colfax&section=00&Well_Type=S&CancelledAPDs=Exclude&PluggedWells=Exclude&SearchLocation=Surface). Figures were produced using MATLAB and GMT (Wessel & Smith, 1991).

Acknowledgments
We thank Justin Rubinstein and an anonymous reviewer for their constructive suggestions. We thank Matt Weingarten, Justin Rubinstein, and Jenny Nakai for their helpful discussions. Private landowners, including the Vermejo Park Ranch, generously hosted seismometers. We thank all the fieldworkers who contributed to the broadband and node arrays used in the study. This research was supported by NSF EAR 1554908. The IRIS DMC is supported by the National Science Foundation under Cooperative Support Agreement EAR-1851048.

References

Allen, R. V. (1978). Automatic earthquake recognition and timing from single traces. *Bulletin of the Seismological Society of America*, *68*(5), 1521–1532. https://doi.org/10.1785/bssa0680051521

Ansari, E., Bidgoli, T. S., & Hollenbach, A. (2019). Accelerated fill-up of the Arbuckle Group aquifer and links to U.S. midcontinent seismicity. *Journal of Geophysical Research: Solid Earth*, *124*, 2670–2683. https://doi.org/10.1029/2018jb016926

ANSS ComCat (2021). *Advanced national seismic system comprehensive earthquake catalog*. Retrieved from https://earthquake.usgs.gov/data/comcat/

Bachmann, C. E., Weimer, S., Goertz-Allmann, B. P., & Woessner, J. (2012). Influence of pore-pressure on the event-size distribution of induced earthquakes. *Geophysical Research Letters*, *39*, L09302. https://doi.org/10.1029/2012GL051480

Baiesi, M., & Paczuski, M. (2004). Scale-free networks of earthquakes and aftershocks. *Physical Review E—Statistical Physics, Plasmas, Fluids, and Related Interdisciplinary Topics*, *69*, 066106. https://doi.org/10.1103/PhysRevE.69.066106

Baltz, E. H. (1965). Stratigraphy and history of the Raton basin and notes on San Luis basin, Colorado-New Mexico. *American Association of Petroleum Geologists Bulletin*, *49*, 2041–2075. https://doi.org/10.1306/a6633882-16c0-11d7-8645000102c1865d

Barbour, A. J., Norbeck, J. H., & Rubinstein, J. L. (2017). The effects of varying injection rates in Osage County, Oklahoma, on the 2016 Mw 5.8 Pawnee earthquake. *Seismological Research Letters*, *88*(4), 1040–1053. https://doi.org/10.1785/0220170003

Barnhart, W. D., Benz, H. M., Hayes, G. P., Rubinstein, J. L., & Bergman, E. (2014). Seismological and geodetic constraints on the 2011 Mw5.3 Trinidad, Colorado earthquake and induced deformation in the Raton Basin. *Journal of Geophysical Research: Solid Earth*, *119*, 7923–7933. https://doi.org/10.1002/2014jb011227

Blackwell, D. D., Richards, M. C., Frone, Z. S., Batir, J. F., Williams, M. A., Ruzo, A. A., & Dingwall, R. K. (2011). *SMU geothermal laboratory heat flow map of the conterminous United States, 2011*. Retrieved from http://www.smu.edu/geothermal

Bollinger, G. A., Adams, M. J., Henrisy, R. F., & Langer, C. J. (1983). The Denver earthquake sequence of March-April 1981. *Seismological Research Letters*, *54*, 3–12. https://doi.org/10.1785/gssrl.54.2.3

Bonner, J. L., Blackwell, D. D., & Herrin, E. T. (2003). Thermal constraints on earthquake depths in California. *Bulletin of the Seismological Society of America*, *93*, 2333–2354. https://doi.org/10.1785/0120030041

Brodsky, E. E., & Lajoie, L. J. (2013). Anthropogenic seismicity rates and operational parameters at the Salton Sea geothermal field. *Science*, *341*(6145), 543–546. https://doi.org/10.1126/science.1239213

Chang, K. W., & Segall, P. (2016). Injection-induced seismicity on basement faults including poroe- lastic stressing. *Journal of Geophysical Research: Solid Earth*, *121*, 2708–2726. https://doi.org/10.1002/2015JB012561

Cochran, E. S., Ross, Z. E., Harrington, R. M., Dougherty, S. L., & Rubinstein, J. L. (2018). Induced earthquake families reveal distinctive evolutionary patterns near disposal wells. *Journal of Geophysical Research: Solid Earth*, *123*, 8045–8055. https://doi.org/10.1029/2018JB016270

Cochran, E. S., Wickham-Piotrowski, A., Kemna, K., Harington, R., Dougherty, S., & Castro, A. P. (2020). Minimal clustering of injection-induced earthquakes observed with a large-n seismic array. *Bulletin of the Seismological Society of America*, *110*(5), 2005–2017. https://doi.org/10.1785/0120200101

COGCC. (2021). *Colorado oil and gas conservation commission*. Retrieved from http://cogcc.state.co.us/data.html#/cogis

Dane, C. H., & Bachman, G. O. (1965). *Geologic map of New Mexico*. U. S. Geological Survey. Scale, 1:500.000.

Dempsey, D., & Riffault, J. (2019). Response of induced seismicity to injection rate reduction: Models of delay, decay, quiescence, recovery, and Oklahoma. *Water Resources Research*, *55*, 656–681. https://doi.org/10.1029/2018WR023587

Dreger, D. S. (2003). TDMT_INV: Time domain seismic moment tensor inversion. In W. H. K. Lee, H. Kanamori, P. C. Jennings, & C. Kisslinger (Eds.), *International handbook of earthquake and engineering seismology, Part B, International Geophysics Series* (Vol. *81*, p. 1627). Academic Press. https://doi.org/10.1016/s0074-6142(03)80290-5

Earle, P. S., & Shearer, P. M. (1994). Characterization of global seismograms using an automatic-picking algorithm. *Bulletin of the Seismological Society of America*, *84*(2), 366–376. https://doi.org/10.1785/bssa0840020366

Ellsworth, W. L. (2013). Injection-induced earthquakes. *Science*, *341*(6142), 1225942. https://doi.org/10.1126/science.1225942

Farrell, S., Husen, S., & Smith, R. B. (2009). Earthquake swarm and b-value characterization of the Yellowstone volcano-tectonic system. *Journal of Volcanology and Geothermal Research*, *188*, 260–276. https://doi.org/10.1016/j.jvolgeores.2009.08.008

Flores, R. M., & Bader, L. R. (1999). *A summary of tertiary coal resources of the Raton Basin, Colorado and New Mexico, chap. SR of fort union coal assessment team, 1999 resource assessment of selected tertiary coal beds and zones in the northern Rocky Mountains and great plains region*. U.S. Geological Survey Professional Paper 1625-A.

Frohlich, C. (2012). Two-year survey comparing earthquake activity and injection-well locations in the Barnett Shale, Texas. *Proceedings of the National Academy of Sciences*, *109*(35), 13934–13938. https://doi.org/10.1073/pnas.1207728109

Frohlich, C., Hayward, C., Rosenblit, J., Aiken, C., Hennings, P., Savvaidis, A., et al. (2020). Onset and cause of increased seismic activity near Pecos, West Texas, United States, from observations at the Lajitas TXAR Seismic Array. *Journal of Geophysical Research: Solid Earth*, *125*(1), e2019JB017737. https://doi.org/10.1029/2019jb017737

Goebel, T. H., & Brodsky, E. E. (2018). The spatial footprint of injection wells in a global compilation of induced earthquake sequences. *Science*, *361*(6405), 899–904. https://doi.org/10.1126/science.aat5449

Goebel, T. H., Weingarten, M., Chen, X., Haffener, J., & Brodsky, E. E. (2017). The 2016 Mw5.1 Fairview, Oklahoma earthquakes: Evidence for long-range poroelastic triggering at >40 km from fluid disposal wells. *Earth and Planetary Science Letters*, *472*, 50–61. https://doi.org/10.1016/j.epsl.2017.05.011

Goebel, T. H. W., Hosseini, S. M., Cappa, F., Hauksson, E., Ampuero, J. P., Aminzadeh, F., & Saleeby, J. B. (2016). Wastewater disposal and earthquake swarm activity at the southern end of the Central Valley, California. *Geophysical Research Letters*, *43*, 1092–1099. https://doi.org/10.1002/2015GL066948

Goebel, T. H. W., Rosson, Z., Brodsky, E. E., & Walter, J. I. (2019). Aftershock deficiency of induced earthquake sequences during rapid mitigation efforts in Oklahoma. *Earth and Planetary Science Letters*, *522*, 135–143. https://doi.org/10.1016/j.epsl.2019.06.036

Gutenberg, B., & Richter, C. F. (1956). Earthquake magnitude, intensity, energy, and acceleration. *Bulletin of the Seismological Society of America*, *46*, 105–145. https://doi.org/10.1785/bssa0460020105

Hainzl, S., & Ogata, Y. (2005). Detecting fluid signals in seismicity data through statistical earthquake modeling. *Journal of Geophysical Research*, *110*, B05S07. https://doi.org/10.1029/2004JB003247

Harte, D. (2010). PtProcess: An R package for modeling marked point process indexed by time. *Journal of Statistical Software*, *35*(8), 1–32. https://doi.org/10.18637/jss.v035.i08

Healy, J. H., Rubey, W. W., Griggs, D. T., & Raleigh, C. B. (1968). The Denver earthquakes. *Science*, *161*(3848), 1301–1310. https://doi.org/10.1126/science.161.3848.1301

Hemborg, T. H. (1998). Spanish Peak Field, Las Animas County, Colorado: Geologic setting and early development of a coalbed methane reservoir in the central Raton Basin. *Colorado Geological Survey*. Resource Series 33, 34p.

Hsieh, P. A., & Bredehoeft, J. D. (1981). A reservoir analysis of the Denver earthquakes: A case of induced seismicity. *Journal of Geophysical Research*, *86*, 903–920. https://doi.org/10.1029/JB086iB02p00903

Johnson, R. B. (1969). *Geologic map of the Trinidad quadrangle, south-central Colorado*. U. S. Geological Survey. Miscellaneous Geologic Investigations Map I-558.

Johnson, R. B., & Wood, H. H., Jr (1956). Stratigraphy of upper cretaceous and tertiary rocks of Raton Basin, Colorado and New Mexico. *American Association of Petroleum Geologists Bulletin*, *40*, 707–721. https://doi.org/10.1306/5ceae400-16bb-11d7-8645000102c1865d

Johnson, R. C., & Finn, T. M. (2001). *Potential for a Basin-Centered Gas Accumulation in the Raton Basin, Colorado and New Mexico*. USGS Bulletin, 2184-B.

Joubert, C., Sohrabi, R., Rubinstein, J. L., Jansen, G., & Miller, S. A. (2020). Injection-Induced Earthquakes Near Milan, Kansas, controlled by Karstic Networks. *Geophysical Research Letters*, *47*(21), 1–9. https://doi.org/10.1029/2020GL088326

Kagan, Y. Y., & Jackson, D. D. (1991). Long-term earthquake clustering. *Geophysical Journal International*, *104*(1), 117–134. https://doi.org/10.1111/j.1365-246X.1991.tb02498.x

Karlstrom, K. E., Crossey, L. J., Hilton, D. R., & Barry, P. H. (2013). Mantle He-3 and CO_2 degassing in carbonic and geothermal springs of Colorado and implications for neotectonics of the Rocky Mountains. *Geology*, *41*, 495–498. https://doi.org/10.1130/g34007.1

Keranen, K. M., & Weingarten, M. (2018). Induced seismicity. *Annual Review of Earth and Planetary Sciences*, *46*(1), 149–174. https://doi.org/10.1146/annurev-earth-082517-010054

Keranen, K. M., Weingarten, M., Abers, G. A., Bekins, B. A., & Ge, S. (2014). Sharp increase in central Oklahoma seismicity since 2008 induced by massive wastewater injection. *Science*, *345*(6195), 448–451. https://doi.org/10.1126/science.1255802

Kissling, E., Ellsworth, W., Eberhart-Phillips, D., & Kradolfer, E. (1994). Initial reference models in local earthquake tomography. *Journal of Geophysical Research*, *99*, 19635–19646. https://doi.org/10.1029/93jb03138

Kothari, S., Shcherbakov, R., & Atkinson, G. (2020). Statistical modeling and characterization of induced seismicity within the Western Canada Sedimentary Basin. *Journal of Geophysical Research: Solid Earth*, *125*, e2020JB020606. https://doi.org/10.1029/2020JB020606

Kraft, T., & Deichmann, N. (2014). High-precision relocation and focal mechanism of the injection-induced seismicity at the Basel EGS. *Geothermics*, *52*, 59–73. https://doi.org/10.1016/j.geothermics.2014.05.014

Langenbruch, C., Weingarten, M., & Zoback, M. D. (2018). Physics-based forecasting of man-made earthquake hazards in Oklahoma and Kansas. *Nature Communications*, *9*, 3946. https://doi.org/10.1038/s41467-018-06167-4

Lei, X., Wang, Z., Su, J., & Su, J. (2019). Possible link between long-term and short-term water injections and earthquakes in salt mine and shale gas site in Changning, south Sichuan Basin, China. *Earth and Planetary Physics*, *3*(6), 510–525. https://doi.org/10.26464/epp2019052

Lei, X., Yu, G., Ma, S., Wen, X., & Wang, Q. (2008). Earthquakes induced by water injection at ~3 km depth within the Rongchang gas field, Chongqing, China. *Journal of Geophysical Research*, *113*. https://doi.org/10.1029/2008JB005604

Li, Y. G., Vidale, J. E., Aki, K., Marone, C. J., & Marone, C. J. (1994). Fine structure of the Landers fault zone: Segmentation and the rupture process. *Science*, *265*, 367–370. https://doi.org/10.1126/science.265.5170.367

Liu, M., Zhang, M., Zhu, W., Ellsworth, W. L., & Li, H. (2020). Rapid characterization of the July 2019 Ridgecrest, California, earthquake sequence from raw seismic data using machine learning phase picker. *Geophysical Research Letters*, *47*, e2019GL086189. https://doi.org/10.1029/2019gl086189

Llenos, A. L., & Michael, A. J. (2013). Modeling earthquake rate changes in Oklahoma and Arkansas: Possible signatures of induced seismicity. *Bulletin of the Seismological Society of America*, *103*, 2850–2861. https://doi.org/10.1785/0120130017

Llenos, A. L., & Michael, A. J. (2016). Characterizing potentially induced earthquake rate changes in the Brawley Seismic Zone, Southern California. *Bulletin of the Seismological Society of America*, *106*(5), 2045–2062. https://doi.org/10.1785/0120150053

Lund Snee, J. -E., & Zoback, M. D. (2020). Multiscale variations of the crustal stress field throughout north America. *Nature Communications*, *11*(1), 1–9. https://doi.org/10.1038/s41467-020-15841-5

Martínez-Garzón, P., Kwiatek, G., Bohnhoff, M., & Dresen, G. (2016). Impact of fluid injection on fracture reactivation at The Geysers geothermal field. *Journal of Geophysical Research: Solid Earth*, *121*, 7432–7449. https://doi.org/10.1002/2016JB013137

Martínez-Garzón, P., Zaliapin, I., Ben-Zion, Y., Kwiatek, G., & Bohnhoff, M. (2018). Comparative study of earthquake clustering in relation to hydraulic activities at geothermal fields in California. *Journal of Geophysical Research: Solid Earth*, *123*, 4041–4062. https://doi.org/10.1029/2017JB014972

McGarr, A. (2014). Maximum magnitude earthquakes induced by fluid injection. *Journal of Geophysical Research: solid earth*, *119*(2), 1008–1019. https://doi.org/10.1002/2013jb010597

Meremonte, M. E., Lahr, J. C., Frankel, A. D., Dewey, J. W., Crone, A. J., Overturf, D. E., et al. (2002). *Investigation of an earthquake swarm near Trinidad, Colorado, August–October 2001*. U.S Geol. Surv. Open-File Rept. 02-0073.

Morgan, P. (2009). A preliminary analysis of geothermal resources in the Central Raton Basin, Colorado, from Bottom-Hole Temperature Data. *GRC Transactions*, *33*, 509–513.

Mousavi, S. M., Ogwari, P. O., Horton, S. P., & Langston, C. A. (2017). Spatio-temporal evolution of frequency-magnitude distribution and seismogenic index during initiation of induced seismicity at Guy-Greenbrier, Arkansas. *Physics of the Earth and Planetary Interiors*, *267*, 53–66. https://doi.org/10.1016/j.pepi.2017.04.005

Nakai, J. S., Sheehan, A. F., & Bilek, S. L. (2017). Seismicity of the rocky mountains and Rio Grande Rift from the EarthScope transportable array and CREST temporary seismic networks, 2008–2010. *Journal of Geophysical Research: Earth Surface*, *122*, 2173–2192. https://doi.org/10.1002/2016JB013389

Nakai, J. S., Weingarten, M., Sheehan, A. F., Bilek, S. L., & Ge, S. (2017). A possible causative mechanism of Raton Basin, New Mexico and Colorado earthquakes using recent seismicity patterns and pore pressure modeling. *Journal of Geophysical Research: Solid Earth*, *122*(10), 8051–8065. https://doi.org/10.1002/2017jb014415

NMOCD. (2021). *New Mexico oil and conservation division*. Retrieved from https://wwwapps.emnrd.state.nm.us/ocd/ocdpermitting/Data/Wells.aspx

Ogata, Y. (1988). Statistical models for earthquake occurrences and residual analysis for point processes. *Journal of the American Statistical Association*, *83*(401), 9–27. https://doi.org/10.1080/01621459.1988.10478560

Omori, F. (1894). On the aftershocks of earthquakes. *J. Coll. Sci. Imp. Univ. Tokyo*, *7*, 111–200.

Papadopulous, S. S., & Associates, Inc (2008). Coalbed Methane Stream Depletion Assessment Study- Raton Basin, Colorado. In *Conjunction with*. Colorado Geological Survey.

Park, Y., Mousavi, S. M., Zhu, W., Ellsworth, W. L., & Beroza, G. C. (2020). Machine learning-based analysis of the Guy-Greenbrier, Arkansas earthquakes: A tale of two sequences. *Geophysical Research Letters*, *47*, e2020GL087032. https://doi.org/10.1029/2020gl087032

Peterie, S. L., Miller, R. D., Intfen, J. W., & Gonzales, J. B. (2018). Earthquakes in Kansas induced by extremely far-field pressure diffusion. *Geophysical Research Letters*, *45*, 1395–1401. https://doi.org/10.1002/2017GL076334

Pillmore, C. L. (1964). *Geologic map of the Catskill SW quadrangle, Colfax County, New Mexico*. U. S. Geological Survey. Open-File Report OF-64-123.

Pillmore, C. L. (1965a). *Geologic map of the Catskill NE quadrangle, Colfax County, New Mexico*. U. S. Geological Survey. Open-File Report OF 65–122.

Pillmore, C. L. (1965b). *Geologic map of the Catskill SE quadrangle, Colfax County, New Mexico*. U. S. Geological Survey. Open-File Report OF-65-121.

Pillmore, C. L. (1969). *Geologic map of the Catskill NW quadrangle, New Mexico and Colorado*. U. S. Geological Survey. Open-File Report OF-66-104.

Pillmore, C. L. (2003). *Geologic map of the Vermejo Park quadrangle, Colfax County, New Mexico, and Las Animas County, Colorado*. U. S. Geological Survey. Open-File Report OF-2003-438.

Raleigh, C. B., Healy, J. H., & Bredehoeft, J. D. (1976). An experiment in earthquake control at Rangely, Colorado. *Science*, *191*, 1230–1237. https://doi.org/10.1126/science.191.4233.1230

Reyes, C., & Wiemer, S. (2020). From ZMAP to ZMAP7: Fast-forwarding 25 years of software evolution. *EGU General Assembly 2020*, EGU2020–18878. Online, 4–8 May 2020. https://doi.org/10.5194/egusphere-egu2020-18878

Roberts, N. S., Bell, A. F., & Main, I. G. (2015). Are volcanic seismic b-values high, and if so when? *Journal of Volcanology and Geothermal Research*, *308*, 127–141. https://doi.org/10.1016/j.jvolgeores.2015.10.021

Rubinstein, J. L., Ellsworth, W. L., McGarr, A., & Benz, H. M. (2014). The 2001–present induced earthquake sequence in the Raton Basin of northern New Mexico and southern Colorado. *Bulletin of the Seismological Society of America*, *104*(5), 2162–2181. https://doi.org/10.1785/0120140009

Saint Louis University (2021). *North America moment tensor: Focal mechanism plots, tables and other compilations*. Retrieved from http://www.eas.slu.edu/eqc/eqc_mt/MECH.NA/

Scanlon, B. R., Weingarten, M. B., Murray, K. E., & Reedy, R. C. (2019). Managing Basin-Scale Fluid Budgets to Reduce Injection-Induced Seismicity from the Recent U.S. Shale Oil Revolution. *Seismological Research Letters*, *90*, 171–182. https://doi.org/10.1785/0220180223

Schoenball, M., Davatzes, N. C., & Glen, J. M. (2015). Differentiating induced and natural seismicity using space-time-magnitude statistics applied to the Coso Geothermal field. *Geophysical Research Letters*, *42*(15), 6221–6228. https://doi.org/10.1002/2015gl064772

Schoenball, M., & Ellsworth, W. L. (2017a). Waveform-relocated earthquake catalog for Oklahoma and southern Kansas illuminates the Regional Fault Network. *Seismological Research Letters*, *88*(5), 1252–1258. https://doi.org/10.1785/0220170083

Schoenball, M., & Ellsworth, W. L. (2017b). A systematic assessment of the spatiotemporal evolution of fault activation through induced seismicity in Oklahoma and Southern Kansas: Induced seismicity evolution in Oklahoma. *Journal of Geophysical Research*, *122*, 10189–10206. https://doi.org/10.1002/2017JB014850

Schoenball, M., Walsh, F. R., Weingarten, M., & Ellsworth, W. L. (2018). How faults wake up: The Guthrie-Langston, Oklahoma earthquakes. *The Leading Edge*, *37*(2), 100–106. https://doi.org/10.1190/tle37020100.1

Schwab, D. R., Bidgoli, T. S., & Taylor, M. H. (2017). Characterizing the potential for injection-induced fault reactivation through subsurface structural mapping and stress field analysis, Wellington Field, Sumner County, Kansas. *Journal of Geophysical Research: Solid Earth*, *122*, 10132–10154. https://doi.org/10.1002/2017jb014071

Segall, P., & Lu, S. (2015). Injection-induced seismicity: Poroelastic and earthquake nucleation effects. *Journal of Geophysical Research: Solid Earth*, *120*, 5082–5103. https://doi.org/10.1002/2015JB012060

Shen, L. W., Schmitt, D. R., Wang, R., & Hauck, T. E. (2021). States of in-situ stress in the Duvernay East Shale Basin and Willesden Green of Alberta, Canada: Variable in-situ stress states effect fault stability. *Journal of Geophysical Research: Solid Earth*, *126*, e2020JB021221. https://doi.org/10.1029/2020JB021221

Skoumal, R. J., Barbour, A. J., Brudzinski, M. R., Langenkamp, T., & Kaven, J. O. (2020). Induced seismicity in the Delaware Basin, Texas. *Journal of Geophysical Research: Solid Earth*, *125*, e2019JB018558. https://doi.org/10.1029/2019JB018558

Skoumal, R. J., & Trugman, D. T. (2021). The proliferation of induced seismicity in the Permian Basin, Texas. *Journal of Geophysical Research: Solid Earth*, *126*, e2021JB021921. https://doi.org/10.1029/2021jb021921

Snoke, J. A. (2003). FOCMEC: Focal mechanism determinations. *International handbook of earthquake and engineering seismology*, *85*, 1629–1630. https://doi.org/10.1016/s0074-6142(03)80291-7

Stoeser, D. B., Green, G. N., Morath, L. C., Heran, W. D., Wilson, A. B., Moore, D. W., & Van Gosen, B. S. (2007). Preliminary integrated geologic map databases for the United States: Central states: Montana, Wyoming, Colorado, New Mexico, North Dakota, South Dakota, Nebraska, Kansas, Oklahoma, Texas, Iowa, Missouri, Arkansas, and Louisiana, *United States Geological Survey, Open File Report (2005-1351)*. Version 1.2. Retrieved from http://pubs.usgs.gov/of/2005/1351/index.htm

Sumy, D. F., Cochran, E. S., Keranen, K. M., Wei, M., & Abers, G. A. (2014). Observations of static Coulomb stress triggering of the November 2011 M5.7 Oklahoma earthquake sequence. *Journal of Geophysical Research: Solid Earth*, *119*, 1904–1923. https://doi.org/10.1002/2013JB010612

Treiman, J. A., Kendrick, K. J., Bryant, W. A., Rockwell, T. K., & McGill, S. F. (2002). Primary surface rupture associated with the *M* 7.1 16 October 1999 Hector Mine earthquake, San Bernardino County, California. *Bulletin of the Seismological Society of America*, *92*, 1171–1191. https://doi.org/10.1785/0120000923

Trugman, D. T., & Shearer, P. M. (2017). GrowClust: A Hierarchical Clustering Algorithm for Relative Earthquake Relocation, with Application to the Spanish Springs and Sheldon, Nevada, Earthquake Sequences. *Seismological Research Letters*, *88*, 379–391. https://doi.org/10.1785/0220160188

Uhrhammer, R. A., & Collins, E. R. (1990). Synthesis of Wood-Anderson seismograms from broadband digital records. *Bulletin of the Seismological Society of America*, *180*(3), 702–216. https://doi.org/10.1785/BSSA0800030702

U. S. Geological Survey. (2021). *National earthquake information center (NEIC)*. Recieved from https://www.usgs.gov/natural-hazards/earthquake-hazards/national-earthquake-information-center-neic?qt-science_support_page_related_con=3#qt-science_support_page_related_con

Utsu, T. (1961). A statistical study on the occurrence of aftershocks. *Geophysical Magazine*, *30*, 521–605.

van Stiphout, T., Kissling, E., Wiemer, S., & Ruppert, N. (2009). Magmatic processes in the Alaska subduction zone by combined 3-D b value imaging and targeted seismic tomography. *Journal of Geophysical Research*, *114*, B11302. https://doi.org/10.1029/2008JB005958

Vasylkivska, V. S., & Huerta, N. J. (2017). Spatiotemporal distribution of Oklahoma earthquakes: Exploring relationships using a nearest-neighbor approach. *Journal of Geophysical Research: Solid Earth*, *122*, 5395–5416. https://doi.org/10.1002/2016JB013918

Verdecchia, A., Cochran, E. S., & Harrington, R. M. (2021). Fluid-earthquake and earthquake-earthquake interactions in southern Kansas, USA. *Journal of Geophysical Research: Solid Earth*, *126*, e2020JB020384. https://doi.org/10.1029/2020jb020384

Walsh, R. R., & Zoback, M. D. (2015). Oklahoma's recent earthquakes and saltwater disposal. *Science Advances*, *1*, e1500195. https://doi.org/10.1126/sciadv.1500195

Wang, K., Ellsworth, W., & Beroza, G. C. (2020). Revisiting the Timpson induced earthquake sequence: A system of two parallel faults. *Geophysical Research Letters*, *47*, e2020GL089192. https://doi.org/10.1029/2020GL089192

Wang, R., Gu, Y. J., Schultz, R., & Chen, Y. (2018). Faults and non-double-couple components for induced earthquakes. *Geophysical Research Letters*, *45*(17), 8966–8975. https://doi.org/10.1029/2018gl079027

Wang, R., Gu, Y. J., Schultz, R., Kim, A., & Atkinson, G. (2016). Source analysis of a potential hydraulic fracturing induced earthquake near Fox Creek, Alberta. *Geophysical Research Letters*, *43*, 564–573. https://doi.org/10.1002/2015GL066917

Wang, R., Schmandt, B., Zhang, M., Glasgow, M., Kiser, E., Rysanek, S., & Stairs, R. (2020). Injection-induced earthquakes on complex fault zones of the Raton Basin illuminated by machine-learning phase picker and dense nodal array. *Geophysical Research Letters*, *46*, e2020GL088168. https://doi.org/10.1029/2020gl088168

Weingarten, M., Ge, S., Godt, J. W., Bekins, B. A., & Rubinstein, J. L. (2015). High-rate injection is associated with the increase in U.S. mid-continent seismicity. *Science*, *348*(6241), 1336–1340. https://doi.org/10.1126/science.aab1345

Wessel, P., & Smith, W. H. (1991). Free software helps map and display data. *Eos, Transactions American Geophysical Union*, *72*(41), 441–441. https://doi.org/10.1029/90EO00319

Wiemer, S. (2001). A software package to analyze seismicity: Zmap. *Seismological Research Letters*, *72*, 373–382. https://doi.org/10.1785/gssrl.72.3.373

Wiemer, S., & Wyss, M. (2000). Minimum magnitude of completeness in earthquake catalogs: Examples from Alaska, the Western United States, and Japan. *Bulletin of the Seismological Society of America*, *90*(4), 859–869. https://doi.org/10.1785/0119990114

Woessner, J., & Wiemer, S. (2005). Assessing the quality of earthquake catalogues: Estimating the magnitude of completeness and its uncertainty. *Bulletin of the Seismological Society of America*, *95*(2), 684–698. https://doi.org/10.1785/0120040007

Woodward, L. A. (1997). Role of regional tectonic analysis in exploration for fracture reservoirs in Cretaceous source rocks of the Raton Basin, New Mexico. *Mountain Geologist*, *34*, 73–80.

Zaliapin, I., & Ben-Zion, Y. (2013). Earthquake clusters in southern California I: Identification and stability. *Journal of Geophysical Research: Solid Earth*, *118*, 2847–2864. https://doi.org/10.1002/jgrb.50179

Zaliapin, I., & Ben-Zion, Y. (2015). Artefacts of earthquake location errors and short-term incompleteness on seismicity clusters in southern California. *Geophysical Journal International*, *202*, 1949–1968. https://doi.org/10.1093/gji/ggv259

Zaliapin, I., & Ben-Zion, Y. (2016a). A global classification and characterization of earthquake clusters. *Geophysical Journal International*, *207*, 608–634. https://doi.org/10.1093/gji/ggw300

Zaliapin, I., & Ben-Zion, Y. (2016b). Discriminating characteristics of tectonic and human-induced seismicity. *Bulletin of the Seismological Society of America*, *106*(3), 846–859. https://doi.org/10.1785/0120150211

Zaliapin, I., Gabrielov, A., Keilis-Borok, V., & Wong, H. (2008). Clustering analysis of seismicity and aftershock identification. *Physical Review Letters*, *101*(1), 018501. https://doi.org/10.1103/physrevlett.101.018501

Zhai, G., Shirzaei, M., Manga, M., & Chen, X. (2019). Pore-pressure diffusion, enhanced by poroelastic stresses, controls induced seismicity in Oklahoma. *Proceedings of the National Academy of Sciences of the United States of America*, *116*(33), 16228–16233. https://doi.org/10.1073/pnas.1819225116

Zhang, M., Ellsworth, W. L., & Beroza, G. C. (2019). Rapid Earthquake Association and Location. *Seismological Research Letters*, *90*(6), 2276–2284. https://doi.org/10.1785/0220190052

Zhu, W., & Beroza, G. C. (2019). PhaseNet: A deep-neural-network-based seismic arrival-time picking method. *Geophysical Journal International*, *216*(1), 261–273.